Gypsum lithofacies and stratigraphic architecture of a Messinian marginal basin (Piedmont Basin, NW Italy)

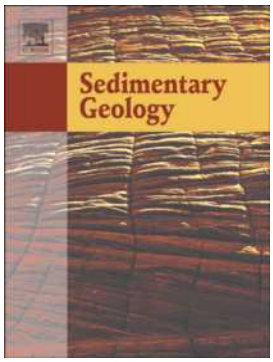

Gypsum lithofacies and stratigraphic architecture of a Messinian marginal basin (Piedmont Basin, NW Italy)

Marcello Natalicchio, Luca Pellegrino, Pierangelo Clari, Linda Pastero, Francesco Dela Pierre

PII: S0037-0738(21)00161-5

DOI: https://doi.org/10.1016/j.sedgeo.2021.106009

Reference: SEDGEO 106009

To appear in: *Sedimentary Geology*

Received date: 21 July 2021

Revised date: 23 September 2021

Accepted date: 25 September 2021

Please cite this article as: M. Natalicchio, L. Pellegrino, P. Clari, et al., Gypsum lithofacies and stratigraphic architecture of a Messinian marginal basin (Piedmont Basin, NW Italy), *Sedimentary Geology* (2021), https://doi.org/10.1016/j.sedgeo.2021.106009

Gypsum lithofacies and stratigraphic architecture of a Messinian marginal basin (Piedmont Basin, NW Italy)

Marcello Natalicchio, Luca Pellegrino, Pierangelo Clari, Linda Pastero, Francesco Dela Pierre*

Dipartimento di Scienze della Terra, Università di Torino, Via Valperga Caluso, 35, 10125 Torino, Italy.

*corresponding author email: francesco.delapierre@unito.it

ABSTRACT

During the Messinian salinity crisis (5.97–5.33 Ma) the Mediterranean was transformed into the youngest salt giant in Earth history. In marginal Mediterranean subbasins, the first stage of the crisis is recorded by up to 16 lithological cycles made up of shale/ gypsum couplets (Primary Lower Gypsum unit, PLG), making a downslope transition to organic-rich shales. Gypsum comprises a wide array of lithofacies, including bottom-grown gypsum, cumulate deposits (i.e., resulting from gypsum nucleation in the water column and subsequent deposition on the seafloor) and the branching selenite lithofacies. The latter appeared synchronously in many sections of the Mediterranean in the 6th PLG cycle (i.e., at about 5.87 Ma). To investigate the still enigmatic stratigraphic architecture of the lateral lithofacies transition from the shallower basin margin to the depocenter and the paleonvironmental modifications driving the development of the branching selenite lithofacies, we carried sedimentological, petrographic and geochemical analyses of the different types of gypsum lithofacies exposed along a margin-to-depocenter transect in the Piedmont Basin (NW Italy), corresponding to the northernmost Mediterranean subbasin. The results of this study suggest

that the lateral and vertical distribution of gypsum lithofacies mostly reflects the position of an oxycline with respect to the seafloor. Bottom grown gypsum (cycles PLG1-PLG5) was deposited on a temporarily oxygenated seafloor above the oxycline in the marginal part of the basin. In the case of cumulate deposits (laminar gypsum and gypsiferous mudstones, cycles PLG6-PLG15), gypsum nucleated within the water column at the oxycline and was eventually deposited on an anoxic seafloor. The branching selenite lithofacies corresponds to a syngenetic product formed below the seafloor at the expenses of cumulate gypsum. Deposition of cumulate gypsum and formation of the branching selenite were controlled by the balance between the rate of sulfate reduction in bottom waters and nucleation of gypsum in the water column. The appearance of cumulate gypsum and the branching selenite from the 6th PLG cycle upwards reflects the intensification of water column stratification in response to increased isolation of the basin.

Keywords: Gypsum, branching selenite, cumulate deposits, water column stratification, Messinian salinity crisis.

1. Introduction

Thick successions of gypsum were deposited in the Mediterranean basin during the Messinian salinity crisis (MSC; 5.97-5.33 Ma), when the Mediterranean was turned into the youngest salt giant in Earth history (Hsü et al., 1973; Krijgsman et al., 1999; Roveri et al., 2014; Flecker et al., 2015). The sedimentary products of the MSC are more than 1 million km^3 of evaporites (carbonate minerals, gypsum, anhydrite and halite) (Ryan, 2008, Haq et al., 2020) that are found in a variety of onland marginal subbasins as well as in offshore basinal areas of Western and Eastern Mediterranean, as suggested by seismic data (Lofi et al., 2011; Raad et al., 2020), (Fig. 1A). Messinian gypsum comprises both in situ-precipitated and

detrital deposits (Roveri et al., 2014). In situ deposits were grouped in two stratigraphic units referred to as the Lower Evaporites (containing also the thick massive halite and K/Mg salts of deep basins and Sicily), and Upper Evaporites (Rouchy and Caruso, 2006). More recently an alternative terminology was proposed, following the three stage model of the MSC events that is mostly based on outcrop studies of key sections from different Mediterranean marginal basins (CIESM, 2008; Manzi et al., 2013; Roveri et al., 2014), including the Piedmont basin (Dela Pierre et al., 2011). According to this model, that is not unanimously accepted by the scientific community (e.g., Meilijson et al., 2019), in situ primary gypsum is ascribed to (a) the Primary Lower Gypsum (PLG) unit, representing the first stage of the MSC (5.97-5.60 Ma; Manzi et al., 2013), and (b) the Upper Gypsum, recording the third stage of the MSC (5.55-5.33 Ma) (Roveri et al., 2014) (Fig. 1B). Detrital, resedimented gypsum was deposited during the second stage of the crisis (5.60-5.55 Ma), forming the Resedimented Lower Gypsum unit that apparently interfingers with halite (Roveri et al., 2014). The PLG unit, the object of this paper, is composed of up to 16 lithological cycles consisting of shale (and marl)/gypsum couplets (Lugli et al., 2010). Deposition of the lithological cycles is interpreted to be controlled by orbitally-driven climate oscillations (precession) (Krijgsman et al., 1999). Shales would be indicative of relatively humid climate during precession minima (insolation maxima), whereas gypsum is thought to reflect more arid conditions during precession maxima (insolation minima) . The PLG unit comprises a variety of gypsum lithofacies whose origin is still debated (see Ortì, 2011): (a) the massive and banded selenite, consisting of vertically-oriented palisades of bottom-nucleated selenite crystals (arrow head or swallow-tail twins, Shearman and Ortì Cabo, 1976); (b) the branching selenite, defined by Lugli et al. (2010) as consisting of *"clear selenite crystals a few centimeters across with their long axis inclined or oriented horizontally grouped into decimeter-large irregular nodules and lenses separated by thin fine-grained carbonate or gypsum laminae"*; and (c) the laminar gypsum,

formerly termed “balatino” (Ogniben, 1957), either representing a in situ deposit of sub-mm gypsum crystals or a fine-grained clastic deposit emplaced by low density gravity flows (Manzi et al., 2005). Across the different Mediterranean subbasins in southern Spain (i.e. Sorbas and Nijar basins), northern Italy (i.e. Piedmont and Vena del Gesso basins) and southern Italy (Sicily), these gypsum lithofacies show a similar stratigraphic stacking pattern (Lugli et al., 2010): the lower five PLG cycles are composed only of the massive and banded selenite lithofacies, whereas from the 6th cycle upwards the branching selenite is also found. In the gypsum layers of the Vena del Gesso, the branching selenite is developed at the top of the massive and banded selenite (Lugli et al., 2010), whereas in Piedmont forms entire beds and is strictly interlayered with laminar gypsum (Dela Pierre et al., 2011). The PLG unit passes laterally, in the intermediate depths and deep basins, to organic-rich shales (Manzi et al., 2007), but the details of such a transition are still poorly known. Still uncertain, moreover, are the depositional mechanisms and the environmental conditions at the origin of the laminar gypsum and the branching selenite lithofacies, especially in light of the apparent synchronous formation of the branching selenite in different Mediterranean marginal subbasins.

This paper integrates previous stratigraphic studies (Dela Pierre et al., 2011) with novel sedimentological, petrographic and geochemical data on the different gypsum lithofacies (massive selenite, branching selenite and laminar gypsum) composing the PLG unit along a margin-to-depocenter transect of a Messinian marginal subbasin located at the northernmost offshoot of the Mediterranean (Piedmont Basin, NW Italy), with the main aims to: (a) provide a detailed description of the gypsum lithofacies, in particular of the still poorly known laminar gypsum and branching selenite; (b) shed light on the paleoenvironmental conditions under which the different lithofacies formed and reconstruct the mechanisms behind the appearance of the laminar gypsum and the branching selenite in the 6th PLG cycle; and (c) discuss the lateral lithofacies transition between the basin margin and the depocenter.

2. Geological setting

During the Messinian the Piedmont Basin (northern Italy) (Fig. 1C) corresponded to a wide wedge-top basin, developed upon an orogenic wedge of Alpine, Ligurian and Adria basement units (Rossi et al., 2009; Mosca et al., 2010; Rossi, 2017). The shallow marginal zones are presently exposed in the southern (Langhe) and northern (Monferrato/Torino Hill) sectors, the latter corresponding to the uplifted sill interposed between the Piedmont Basin and the NW termination of the larger Apennine foredeep (present-day Po plain). The depocenter of the basin is buried below Pliocene and Quaternary deposits but is well imaged by seismic data (Ghielmi et al., 2019). The Messinian succession (Fig. 1D) starts with outer shelf to slope fine-grained sediments (Sant'Agata Fossili Marls, Tortonian-lower Messinian) that record progressive restriction of the basin before the onset of the MSC (Sturani, 1973; Sturani and Sampò, 1973; Violanti et al., 2013). At the basin margins this unit is overlain by in situ sulfate evaporites of the PLG unit, representing the first stage of the MSC (5.97-5.60 Ma; Dela Pierre et al., 2011). The PLG unit exhibits a lithological cyclicity interpreted to reflect precession-driven climate oscillations (Fig. 2), as elsewhere in the Mediterranean. Towards the basin depocenter, the gypsum layers make a lateral transition to shales, marls and carbonate-rich layers (Fig. 1D), representing deeper water equivalents of gypsum (Dela Pierre et al., 2012). The PLG unit and its lateral equivalents are overlain by resedimented and chaotic gypsum deposits (Valle Versa Chaotic Complex; Irace et al., 2005; Castellania Chaotic complex; Ghielmi et al., 2019), equivalent to the Resedimented Lower Gypsum unit deposited in many Mediterranean subbasins during the second stage of the MSC (5.60-5.55 Ma; Roveri et al., 2014), (Fig. 1D). In the Piedmont Basin the Messinian succession is closed by fluvio-deltaic and lacustrine deposits (Cassano Spinola Conglomerates), recording the third MSC stage (5.55-5.33 Ma; Fig. 1C). Deposition of Zanclean marine clays and marls

(Argille Azzurre Formation) marks the end of the salinity crisis at 5.33 Ma (Trenkwalder et al., 2008; Violanti et al., 2011).

2.1 The PLG unit in the Piedmont basin

Three subunits (A to C from bottom to the top) were distinguished in the Piedmont Basin according to the prevailing gypsum lithofacies (Dela Pierre et al., 2011) (Fig. 3). In all the subunits, the gypsum layers are interbedded with shales (not described in this paper), forming shale/gypsum couplets which are assumed to correspond to precessional cycles. Subunit A is composed of vertically oriented selenite crystals and includes up to five gypsum beds belonging to cycles PLG1 to 5. The gypsum beds are up to 10 m thick. Their number and thickness decreases from SW to NE, i.e., from the basin margin to the depocenter (Fig. 3). Subunit B includes a single gypsum beds (7-10 m thick) belonging to cycle PLG6 and known as Sturani key-bed (SKB) (Dela Pierre et al., 2011). The SKB represents a distinct marker bed that can be physically correlated from the margin to the distal part of the basin. (Fig. 3). The SKB is composed of two lithofacies that are not observed in the underlying subunit A: laminar gypsum and branching selenite (the latter formerly described as nodular gypsum and "embrichitic" structures) (Sturani, 1973). In the more distal sector of the basin (Govone section, the SKB passes to shales. Subunit C overlies the SKB and comprises up to 9 gypsum beds, about 1 m thick, composed of gypsiferous mudstones (Fig. 3). Subunit C is not present at the basin margins, since it is truncated at the top by an erosional surface (Fig. 3) corresponding to the Messinian erosional surface (Dela Pierre et. al., 2011. In the more distal part of the basin (Govone section) subunit C is the only unit recognizable and directly overlies the Sant'Agata Fossili Marls. In this section, the upper part of the Sant'Agata Fossili Marls is time equivalent of subunits A (cycles PLG1-5) and B (cycle PLG6) (Dela Pierre et al., 2016; Gennari et al., 2020) (Fig. 3).

3. Materials and methods

Field studies of the lithological and sedimentological features of gypsum lithofacies were conducted along a SW-NE transect, representing the transition from the basin margin to the depocenter of the Piedmont Basin (Dela Pierre et al. 2011). The following sections were revisited (Fig. 1C, D): Arnulfi (43°37'06''N; 7°53'41''E), Pollenzo (44°41'08''N; 7°55'33''E) and Govone (44°48'09''N; 8°07'33''E); the Monticello (44°42'39''N; 7°57'39''E) and Castagnito (44°45'44''N; 8°03'07''E) sections were studied for the first time. More detailed observations were done in the Pollenzo section, where the PLG unit is exposed entirely. In the other sections the outcrops are frequently covered by vegetation or the presence of unstable cliffs corresponding to ancient quarry fronts, 10 m high and 20 m wide (Arnulfi) makes field operations dangerous.

A total of 54 oriented samples (15 from Arnulfi, 30 from Pollenzo, 4 from Castagnito and 5 from Govone) were taken from the various gypsum lithofacies for petrographic observations. Thirty polished slabs, 28 petrographic thin sections and 30 thin slices (~1 mm thick) produced by cleaving the selenite crystals along the main (010) cleavage surfaces with a razor blade, were obtained from the most representative samples and studied with transmitted, reflected, and UV-visible light microscopy, using a Leika DM 2700 P microscope with excitation filters 340-380 Nm. Eight polished carbon-coated thin sections were studied for semi-quantitative elemental analyses and backscattered electron imagery (BSEI) using a JSM-IT300LV scanning electron microscope (SEM) equipped with an energy-dispersive EDS Oxford Instruments Link Systems (Department of Earth Sciences, University of Torino). Twenty-five samples of the branching selenite, laminar gypsum and gypsiferous mudstone lithofacies were studied by SEM for morphological analyses. Four samples were also analysed with a FESEM Tescan S9000G microscope at the Centre for Nanostructured

Interfaces and Surfaces of the University of Torino. X-Ray Powder Diffraction (XRPD) analyses were performed on 9 samples of laminar gypsum and gypsiferous mudstones to test for the presence of dolomite, using a Rigaku MiniFlex 600 benchtop X-ray diffractometer. A semi-quantitative analysis was performed applying the RIR (Reference Intensity Ratio) method based on the ratio of the intensities of the phases recognized into the sample with respect to the intensity of a "virtual corundum" (I/Ic). An aliquot of the same powder samples prepared for XRPD analyses was selected to assess the isotopic composition of dolomite. Carbon and Oxygen stable isotope analyses were performed at the Department of Earth Sciences, University of Milan, using an automated carbonate preparation device (Gasbench II) and a Thermo Fisher Scientific Delta V Advantage continuous flow mass spectrometer. The isotope compositions are expressed in the conventional delta notation calibrated to the Vienna Pee-Dee Belemnite (V-PDB) scale. The Total Organic Carbon (TOC) contents of 18 samples representing the laminar gypsum, branching selenite and gypsiferous mudstones lithofacies from the Pollenzo section were determined at the Institute for Geology of the University of Hamburg, using a LECO SC-144DR Carbon Analyzer equipped with an infrared detector.

4. Results

4.1 Field observations

4.1.1 Subunit A (Cycles PLG1-5)

This subunit reaches the maximum thickness (30 m) at the basin margin (Arnulfi section, Fig. 3), The lower three beds are made up of the massive selenite lithofacies, consisting of dm-sized bottom-grown selenite crystals (Fig. 4A, B); with a uniform size throughout the bed. The 4th and 5th beds are composed of the banded selenite lithofacies, i.e cm-thick palisades of twinned crystals separated by mm-thick clay layers (Dela Pierre et al., 2011) (Fig. 4C). In the

more distal Pollenzo section, only two layers of massive selenite, up to 1.5 m thick (Figs. 3, 4A), are present, overlying a cyclic succession of shales and marls belonging to the Sant'Agata Fossili Marls (Fig. 3). Previous studies (Lozar et al. 2018) showed that these thin gypsum beds correspond to the 4th and the 5th PLG beds (banded selenite) of the Arnulfi section and that the underlying shale/marl couplets of the Sant'Agata Fossili Marls are the "deep" water equivalents of the lower three marginal PLG cycles. Basinwards (Fig. 3), subunit A is represented by one (visible) bed of massive selenite (Monticello section) and by isolated cones of gypsum growing in dolomite-rich laminated silty clays (Castagnito section; Fig. 4D). In the more distal Govone section, subunit A passes laterally to dolomite-rich marls (Sabino et al., 2021).

4.1.2 Subunit B (Cycle PLG 6)

Subunit B corresponds to the SKB. The thickness of this layer decreases from 10 m at the basin margin (Arnulfi section) to about 7 m in the more distal part of the basin (Castagnito section) section. At Govone the SKB is not present (Fig. 3). The SKB is composed of the laminar gypsum and branching selenite lithofacies (Fig. 5). Laminar gypsum consists of alternating gypsum-rich (1-2 mm thick) and clay-rich (100-200 m thick) laminae (Figs. 5C, 6A-D), locally organized in dm-thick packets separated by cm-thick clay-rich layers (Fig. 6C). At the outcrop scale the laminae can be followed laterally for tens of metres. No sedimentary structures related to tractive bottom currents (e.g., cross lamination) or oscillatory flows (e.g., hummocky cross stratification) have been observed. In the laminar gypsum, plant remains are abundant and insect remains (dragonfly larvae) have been documented (Sturani, 1973).

The branching selenite lithofacies consists of m-scale flattened cones (Fig. 7A-C) growing in the laminar gypsum. In section perpendicular to bedding, the larger cones appear

asymmetrical, with one side (branch) more developed than the other (Fig. 7B). Branches up to 8 m long and 1.5 m high have been observed in the studied sections (Figs. 5A, 7B, 8A). These large branches form an angle of ~10° with respect to the bedding plane (Fig. 7B). In plain view, the cones show a circular to elliptical shape (Fig. 7D). The cones are composed of clusters of dm-sized nodular aggregates (Figs. 5C, 6A), in turn formed by mm-to cm sized prismatic and twinned gypsum crystals with their long axis inclined or oriented horizontally (Fig. 7E, F). The nodular aggregates are here referred to as the "elemental units" of the branching selenite lithofacies. Within the nodular aggregates, the crystals show a radial distribution (Fig. 7F). The excellent outcrop conditions of the SKB in Pollenzo, where it can be observed on cuts both parallel and perpendicular to the bedding, allowed the reconstruction of the stratigraphic relationships between the branching selenite and the laminar gypsum (Fig. 8A). In most cases, laminae are disrupted and deformed around the nodular aggregates ("elemental units") (Fig. 8B). However, thin lamina packets can also be traced within the branches or drape the upward termination of larger cones (Fig. 8C).

4.1.3 Subunit C (Cycles PLG 7-15)

The gypsum layers of subunit C are up to 3 m thick and shows gradational lower and upper boundaries with the interbedded mudstones. They are composed of gypsiferous mudstones consisting of the alternation of gypsum-poor and gypsum-rich laminae (Fig. 9A). These sediments differ from the laminar gypsum for the higher terrigenous content. The boundary between the types of laminae is transitional, through the gradual increase in the content of gypsum crystals. The gyspiferous mudstones enclose dm-sized conical structures (Fig. 9A, B), with horizontally oriented crystals (Fig. 9C). These features, up to 10 cm high and 70 dm large, are analogous to the cones observed in the SKB but never reach the size of the latter.

4.2. Gypsum microfacies

4.2.2: Vertically-oriented selenite crystals (Subunit A)

In both the massive and banded selenite lithofacies, the re-entrant angle of the twins is typified by a mm-thick lamination given by the alternation of dark turbid laminae, rich in solid inclusions, and clear lighter laminae in which the latter are scarce or absent (Fig. 10A, B). Solid inclusions are represented by fecal pellets, autofluorescent clay-rich aggregates representing marine snow floccules (Fig. 10C), and filamentous microfossils interpreted as remains of colorless sulfide-oxidizing bacteria (Dela Pierre et al., 2015; Natalicchio et al., 2021). Abundant and well-preserved remains of marine planktic diatoms, including the nano-sized *Thalassiosira* cf. *oceanica* and rarer reworked benthic diatoms, were observed in the lower two cycles (Pellegrino et al., 2021).

4.2.2 Laminar gypsum and branching selenite (Subunit B)

In the laminar gypsum the alternation of gypsum-rich- and clay-rich laminae observed in outcrop is clearly recognizable under the microscope (Fig. 11A, B). The gypsum-rich laminae are composed of a mosaic of interlocked rhombohedral to acicular crystals ranging in size from a few µm to some hundreds of µm (Fig. 11C). The crystals are limpid, devoid of solid inclusions and are randomly distributed on the lamina surface (Fig. 11D). The clay-rich laminae show a bright autofluorescence when exposed to UV-light (Fig. 11E), which indicates high contents of organic matter. Other common components are silt-sized terrigenous grains (mica flakes, quartz and feldspar) and tiny (2-20 µm) pyrite framboids (Fig. 11F). The clay-rich laminae contain spheroidal dolomite microcrystals ranging in size from 1 to 5 µm, often typified by a hollow core (Fig. 11G, H). Quantification of the dolomite contents of this lithofacies from XPRD data was not possible (Table 1) because of the overlapping of dolomite and gypsum main diffraction peaks.

When the branching selenite lithofacies is observed on cuts perpendicular to the bedding the "elemental units" of this lithofacies appear as transparent nodular-like gypsum aggregates (Fig. 12A). These aggregates are separated by sub-mm thick layers of autofluorescent clay-rich sediment including spheroidal dolomite microcrystals (Fig. 12B). The nodular aggregates are composed of mm- to cm-sized densely interlocked prismatic and twinned crystals that give rise to a sutured mosaic (Fig. 12A, C). On cuts parallel to the bedding, the crystals show a unidirectional orientation (Fig. 12C). In the aggregates grouped to form larger asymmetrical cones, the long axis of the crystals is preferentially oriented parallel to the elongation of the branches (Fig. 12D). The gypsum crystals show a concentric zoning marked by a fluorescent core surrounded by a not-fluorescent rim (Fig. 12E, F). The core is rich in solid inclusions, including fluorescent loose peloidal sediment, individual pellets (Fig. 12F), gypsum crystals identical to those observed in the laminar gypsum lithofacies (Fig. 12G), terrigenous grains and dolomite microcrystals, i.e., the same components of the clay-rich laminae in the laminar gypsum. Strings of fluorescent fine-grained sediment are observed between the nodular aggregates (Fig. 12A, B). This sediment appears to have been deformed by the displacive growth of the nodular aggregates.

4.2.3 Gypsiferous mudstones (Subunit C)

The gypsiferous mudstones of subunit C consist of alternation of gypsum-poor and gypsum-rich laminae. The gypsum-rich laminae are 1.5 to 2 mm thick and are composed of equant to prismatic limpid crystals, already described in laminar gypsum, mixed with clay and silt-sized terrigenous grains (mica, quartz, feldspars) (Fig. 13A). The gypsum-poor laminae, 150-200 m thick, show a bright autofluorescence when exposed to UV-light and are typified by high contents of spheroidal dolomite microcrystals (up to 30 wt%, Table1). The gypsiferous mudstones show evidences of modification of the original depositional fabric; two end

members can be distinguished: (a) the original lamination of the sediment is still recognizable, but laminae are deformed by the overgrowth of gypsum crystals (Figs 13A). These crystals show prismatic habit, are isolated in the sediment and range in size from 1.5 to 3 mm (Fig. 13A). Larger crystals are found along the lamina boundaries; and (b) the original fabric has been obliterated and the bed is composed of mm-scale interlocked crystals forming cm-scale nodular aggregates (Fig. 13B) enclosed in an autofluorescent and dolomite-rich fine-grained matrix. As described for the branching selenite lithofacies, aggregates can be grouped into larger, dm-sized cones (Fig. 9).

4.3. TOC contents and bulk rock C and O stable isotope composition

The TOC contents of gypsum beds of subunit B (branching selenite and laminar gypsum) and C (gypsiferous mudstones) from the Pollenzo section ranges from 0.1 to 2 wt% (Table 1). Laminar gypsum and gypsiferous mudstones show the highest TOC contents (ranging from 1 to 2 wt%), with small differences between the two subunits. The ^{13}C values of dolomite ($^{13}C_{dol}$) ranges from –4.2 to +0.1‰ PDB, whereas the $^{18}O_{dol}$ values range from –5.0 to +4.2 ‰ PDB (Table 1).

5. Discussion

5.1 Modes of gypsum deposition

5.1.1 Vertically-oriented selenite crystals (subunit A)

The vertically-oriented selenite crystals were deposited on a bottom overlain by calcium and sulfate saturated brines (Fig. 14A). The large and constant size of the selenite crystals that typifies the massive selenite lithofacies suggests a relatively low degree of supersaturation of the brines, allowing the crystals to grow larger (Ortì, 2011). In contrast the smaller crystals in the banded selenite lithofacies (found at the basin margin in the 4th and 5th PLG cycle) reflect

an increase in supersaturation of bottom brines, enhancing the nucleation of crystals and therefore more competition for space among the nuclei (Lugli et al., 2010). The lamination in the re-entrant angle of the twins observed in both massive and banded selenite lithofacies (Fig. 10) possibly reflects short-term (annual? seasonal?) climate oscillations causing cyclic changes of gypsum saturation state in the water mass intercepting the sea floor. During phases of saturation, gypsum growth incorporated sediment and biogenic material accumulated on the top of the crystals during the previous unsaturated phase (turbid laminae) and generated the inclusion-free overgrowths (clear laminae). Gypsum deposition occurred when the sea bottom was oxygenated (Garcia Veigas et al., 2018); oxygenation hampered the activity of sulfate-reducing bacteria able to promote gypsum undersaturation through sulfate consumption (e.g., Bąbel, 2007; De Lange and Krijgsman, 2010). No clear depth indications are provided by these facies, due to the absence of modern analogues. The assignment of the filamentous fossils to colorless sulfide-oxidizing bacteria like *Beggiatoa* and *Thioploca* (Natalicchio et al., 2021) do not provide any depth constraint, since these prokaryotes can live in a wide range of water depth, from bathyal to peritidal settings (e.g. Bailey et al., 2009). In the selenite crystals of cycles PLG1 and 2, the massive occurrence of planktic nano-sized diatoms (*Thalassiosira* sp. *oceanica*) nowadays thriving in coastal to open ocean waters agrees with the notion that bottom-grown gypsum does not necessarily reflect shallow depositional conditions (Pellegrino et al., 2021).

5.1.2 Laminar gypsum and large branching selenite cones (subunit B)

Laminar gypsum, has been described from several Messinian (Hardie and Eugster 1971; Schreiber et al., 1977; Marsaglia and Tribble, 1999; Lugli et al., 2015) and Badenian (Bąbel, 1999) basins as well as from Miocene lacustrine deposits from Spain (Ortì et al., 2014). The laminar gypsum lithofacies was interpreted either as a primary in situ precipitate, or as a

detrital deposit emplaced by low density turbidity currents (Schreiber and El Tabakh, 2000). The latter interpretation is based on the occurrence of soft sediment deformation, bottom current structures (i.e., cross lamination), normal grading, smoothed and rounded crystal boundaries or broken crystals (e.g., Hardie and Eugster, 1971; Bąbel, 1999; Schreiber and El Tabakh, 2000). In the studied case, features indicative of a detrital origin are totally absent. On the contrary, the following evidence indicates that laminar gypsum represents an in situ cumulate deposit, resulting from gypsum nucleation at the top or within the water column and subsequent deposition on the seafloor (Hardie and Lowenstein, 2004; Lugli et al., 2015): (a) the fine lamination and lateral continuity of the gypsum laminae and their cyclic alternation with fine-grained settling material (clay, silt, organic matter) (Fig 5), suggesting that the seafloor was periodically draped by a "pelagic" rain of crystals (Fig. 14B); and (b) the absence of solid inclusions in the crystals, that agrees with nucleation in the water column. The varved aspect of this lithofacies suggests the influence of short-term climate oscillations from more arid (gypsum-rich laminae) to more humid (clay-rich laminae) conditions. Every lamina can be the product of a distinct seasonal sedimentary episode, as documented in modern salinas (e.g., Ortì et al., 1984) or inferred from Messinian gypsum cumulate deposits (Manzi et al., 2012).

The nucleation of tiny gypsum crystals at the top of the water column or within the latter requires high supersaturation conditions favouring the formation of new nuclei, inhibiting them from growing larger (i.e., homogeneous nucleation; Alimi et al., 2003; Alimi and Gadri, 2004; Reiss et al., 2017). High supersaturation may be favoured by: (a) strong seasonal evaporation, which also increases the salinity of surface waters (e.g., Bąbel and Schreiber, 2014) and promotes the nucleation of gypsum at the air-water interface (e.g., Schreiber and El Tabakh, 2000); or (b) mixing of water masses of different chemical composition and density in stratified basins, which can promote gypsum precipitation in the water column

even from a brine that was undersaturated with respect to gypsum before mixing ("salting out" effect; Raup, 1982; Bąbel and Bogucki, 2007). Mixing occurs at the pycnocline (Raup, 1982) which commonly coincides with an oxycline separating an oxygenated upper water layer from an anoxic, denser lower layer, as observed in both modern (Wakehamn et al., 2007) and ancient stratified basin (e.g., Sabino et al., 2021, and reference therein). An additional mechanism known to increase sulfate concentration and gypsum precipitation is the oxidation of sulfide accumulated in organic-rich bottom sediments through bacterial sulfate reduction and diffused upward in the water column until it reaches oxygenated waters above the oxycline (e.g., Tiffany et al., 2007). This process was described in the Salton Sea, a Californian hypersaline lake where gypsum crystals form periodically in the water column (Ma et al., 2020).

Nucleation at the air-water interface and the preservation of settling gypsum at the bottom would imply that the entire water column was saturated; such conditions are consistent with a very shallow basin (i.e., few meters), but it is rather unlikely for the studied deposits since: (a) the absence of physical and paleobiological evidence of very shallow water conditions, such as desiccation features, structures related to tractive bottom currents or bird footprints. These features were instead described in very shallow water laminar gypsum deposits from other Messinian Mediterranean subbasins, such as the "balatino" gypsum from Sicily (Hardie and Eugster 1971) and the Marmara gypsum from Cyprus (Manzi et al., 2016); and (b) the high lateral continuity of the SKB, pointing to uniform depositional conditions across the basin, in line with a relatively deep basin, although a reliable depth estimate is not possible. Therefore, it is reasonable to assume that gypsum nucleated within the water column, at the oxycline of a stratified basin, through brine mixing (Raup, 1982), reoxidation of sulfide, or a combination of the two.

Deposition of laminar gypsum from settling crystals mixed with fine-grained sediment was associated with the formation of the branching selenite. This lithofacies was considered as a bottom grown structure (Lugli et al., 2010) comparable with the subaqueous selenite supercones described in the Sorbas basin (Spain) by Dronkert (1985). The horizontal crystal arrangement was explained with a depressed pycnocline (close to the sea floor), hampering the vertical growth of the crystals (Lugli et al., 2010). The same interpretation was proposed for the branching selenite of the Piedmont Basin studied here (Dela Pierre et al., 2011). However, revisitation of this lithofacies through the field and petrographic analyses presented here reveals that: (a) the crystals of the branching selenite include abundant solid inclusions, which implies their initial poikilotopical growth *within* the sediments; (b) the crystals commonly show a fluorescent core and a limpid non-fluorescent rim devoid of solid inclusion (Fig. 12F), which suggests subsequent overgrowth within the sediments, to form nodular aggregates of interlocked crystals representing the "elemental units" of the branching lithofacies; and (c) at the contact with the nodular aggregates of the branching selenite the laminae of laminar gypsum are bended or even disrupted, suggesting that the crystals continued to grow displacively cannibalizing part of the laminar gypsum crystals and pushing away the enclosing laminated sediment that is now squeezed between the nodular aggregates. These observations suggest that the "elemental units" composing the branching selenite lithofacies actually grew below the sediment water interface, *within* a sediment consisting of a mixture of "pelagic" gypsum crystals, clay and organic matter, i.e, the laminar gypsum (). The fact that locally laminar gypsum and clay-rich layers drape the larger branches (Fig. 8C), suggests that the topmost part of the cones locally reached the seafloor, forming low-relief positive structures draped by particularly intense episodes of accumulation of pelagic rain of gypsum. The asymmetric growth of these structures was explained with the presence of flowing brines causing the preferential growth of the crystals upstream (Bąbel and Bogucki,

2007; Lugli et al., 2010). The absence of tractive current structures in laminar gypsum suggests, however, that brines were not able to move the loose sediment deposited at the sea bottom.

Abundant dolomite microcrystals were observed in the fluorescent laminae of laminar gypsum and around the nodular aggregates in the branching selenite lithofacies (Fig. 11G, H). The spheroidal habit and hollow core of the dolomite microcrystals and the slightly ^{13}C depleted isotope composition of the sediment (^{13}C values –2.4‰ in average) agree with a microbial origin of dolomite (Fontes et al. 1987; Warthmann et al., 2000; Van Lith et al., 2003; Lindtke et al., 2011). The presence of organic matter in the laminar gypsum may suggest that dolomite precipitation was induced by organoclastic bacterial sulfate reduction (Petrash et al., 2017). This process increases alkalinity, and favours the precipitation of ^{13}C depleted carbonate minerals, including dolomite (e.g., Vasconcelos et al., 1995; Sanz-Montero et al., 2009; Bontognali et al., 2012). In addition, such process releases hydrogen sulfide that, reacting with iron, can sink as pyrite (that is actually abundant in the laminar gypsum, see Fig. 11F). Since sulfate reducing bacteria are prevalently anaerobic heterotrophs (e.g., Londry and Des Marais, 2003), it is very likely that the branching selenite grew in anoxic pore waters and that deposition of laminar gypsum took place when the sea bottom was anoxic. The formation and preservation of gypsum in such conditions is in contrast with the notion that bacterial sulfate reduction decreases sulfate concentration, ultimately causing gypsum dissolution (e.g., Bąbel, 2007; De Lange and Krijgsman, 2010). However, gypsum supersaturation can be maintained even in a sulfate reducing environment, if the sulfate sink via microbial reduction is smaller than the supply of sulfate from other sources (e.g., Torfstein et al., 2005). In the case studied here, calcium and sulfate ions could have been continuously shuttled to bottom waters by the settling of solid gypsum microcrystals nucleated in the water column (e.g., Torfstein et al., 2005). These crystals were initially

susceptible to dissolution in the unsaturated lower water column and seafloor. However, when the rate of gypsum nucleation was high, sulfate consumption by microbial sulfate reduction below the oxycline was outweighted by sulfate replenishment through dissolution of solid gypsum. In these conditions, saturation at the sea bottom was immediately attained and maintained, allowing accumulation of tiny crystals forming the gypsum lamina (Fig. 14B, step 1). In contrast, when nucleation of gypsum in the water column was limited or absent and the supply of organic matter enhanced, sulfate removal was not balanced by sulfate replenishment by the pelagic gypsum rain. These conditions, that coincide with the formation of the clay (and dolomite)-rich lamina, favoured the momentary undersaturation of the lower water column and at the seafloor, with consequent dissolution of the rare gypsum crystals settling down from the oxycline and of the crystals deposited during the previous phase (Fig. 14B, step 2). When the pelagic gypsum rain resumed, saturation at the sea bottom was again attained and calcium and sulfate ions previously provided by dissolved crystals to interstitial brines could precipitate, promoting the syngenetic growth and further enlargement of the crystals observed in the nodular aggregates of the branching selenite lithofacies (Fig. 14B, step 3). Repetition of this mechanism through time drove the formation of clusters of aggregates, that could locally reach the seafloor and be sealed by pelagic gypsum during intervals of enhanced nucleation in the water column. On the contrary, in the distal deeper portions of the basin, reduced shuttling of gypsum microcrystals and enhanced bacterial sulfate reduction hampered gypsum preservation (laminar gypsum) and nucleation in the shallow subsurface (branching selenite; Fig. 14B).

In conclusion, we propose that the branching selenite lithofacies is a syngenetic product formed within the sediment, at the expenses of gypsum crystals nucleated in the water column and deposited at the seafloor. These crystals acted as shuttles of calcium and sulfate ions that fostered gypsum deposition in reducing pore waters.

5.1.3 Gypsiferous mudstones and small branching selenite cones (subunit C)

Gypsiferous mudstones share many characteristics with laminar gypsum (lamination, lateral continuity of the laminae, absence of evidence of bottom currents) and are interpreted as cumulate deposits. However, in the gypsiferous laminae the pelagic gypsum crystals are mixed with clay and organic matter. Since the TOC contents are the same as in the SKB (~ 1.5% in average) (Table1), mixing is most likely due to reduced nucleation of gypsum in the water column and enhanced input of clay in the basin, rather than to increased flux of organic matter (Fig. 14C). As described for subunit B, undersaturation of the lower water column and at the seafloor following unbalanced bacterial sulfate reduction, drove dissolution of pelagic gypsum. The subsequent saturation of interstitial brines promoted the syngenetic growth of gypsum crystals in bottom sediments, deforming the lamination and eventually forming nodular aggregates of interlocked crystals ("elemental units") that were grouped together to form the observed cones. Interestingly, gypsum beds of subunit C are thinner than the SKB and large cones are not observed. Such a change reflects most likely the reduced availability of gypsum settling down through the water column, whose dissolution provided calcium and sulfate ions for the growth of crystals in the sediment.

5.2 Mechanisms controlling the distribution of gypsum lithofacies

The progressively younger ages of the first gypsum bed from the basin margin to the depocenter defines an overall progradational stacking pattern reflecting shallowing of the basin from the base to the top of the PLG unit and the consequent shift of gypsum deposition basinwards. This shallowing-upward trend is shared with other PLG marginal subbasins (Vena del Gesso; Lugli et al., 2010; Reghizzi et al., 2018; Sorbas; Roveri et al., 2020).

At the onset of the MSC, bottom grown selenitic gypsum (subunit A) was deposited in the shallowest part of the Piedmont basin (Arnulfi section), whereas marls with filamentous microfossils (Dela Pierre et al, 2012) or rich in dolomite (Sabino et al., 2021) formed at intermediate depth and in the deepest parts of the basin, respectively (Pollenzo and Govone sections). Such lateral facies change was interpreted to reflect the stratification of the water column and the position of the oxycline with respect to the seafloor (Sabino et al., 2021). Bottom grown selenitic gypsum (massive selenite lithofacies) formed only above the oxycline, in mixed and periodically oxygenated calcium and sulfate saturated waters, not affected by bacterial sulfate reduction at times of gypsum precipitation (Fig. 14A). In the specific case where the oxycline intercepted the sea bottom, suboxic conditions prevailed favouring, the growth of microbial mats dominated by sulfide-oxidizing bacteria (Natalicchio et al., 2017). In the deeper sector of the basin, the sea bottom was below the oxycline and bottom grown gypsum did not form, since intense bacterial sulfate reduction (in this case not balanced by "pelagic" gypsum deposition) caused gypsum undersaturation and the formation of authigenic dolomite (Bąbel and Bogucki, 2007; De Lange and Krijgsman, 2010; Sabino et al., 2021). The onset of gypsum deposition in the distal parts of the basin (Pollenzo, Monticello and Castagnito sections) coincides with the vertical facies change from massive (cycle PLG3) to banded selenite (cycle PLG4) at the basin margins. Such a change reflects most likely shallowing of the basin, enhancing supersaturation in the shallowest part and the shifting of the oxycline basinwards. Accordingly, gypsum could start to grow on the previously suboxic or anoxic seafloor. The "distal" selenitic gypsum layers are however thinner and discontinuous (at Castagnito) compared to their marginal counterparts (Fig. 3). Such thickness and lateral continuity reduction possibly results from exhaustion of dissolved calcium and sulfate ions in the distal bottom brine, following massive gypsum precipitation at the basin margins.

The appearance of laminar gypsum and the branching selenite lithofacies (Fig. 14B) reflects a significative paleonvironmental and paleohydrological change at about 5.87 Ma (6th PLG cycle). Interestingly, the branching selenite lithofacies apparently formed synchronously in the 6th PLG cycle in sections located several hundreds of km apart (SE Spain, Sicily, Northern Apennines, Piedmont Basin) (Lugli et al., 2010). This event was possibly related to the reduction of the inflows of oceanic waters and/or to increasing riverine runoff in marginal Mediterranean sub-basins (Reghizzi et al., 2018). Deposition of the 6th PLG cycle correlates with an eccentricity minimum (Manzi et al., 2013), associated with a cooling phase and global sea-level fall (Miller et al., 2011; Van der Laan et al., 2012). These processes, along with ongoing tectonic restriction of the hydrological exchanges with the Atlantic Ocean (e.g., Flecker et al., 2015; Capella et al., 2018) resulted in further restriction of the Mediterranean Sea (e.g., Reghizzi et al., 2018) that consequently became more sensitive to the influx of freshwater from river discharge (or even from the Paratethys; Grothe et al., 2020). An effect of freshwater inflows was the intensification of water column stratification (e.g., Simon and Meijer, 2017). In the Piedmont basin enhanced stratification was associated with the rise of the oxycline in the water column, that led to homogeneous environmental conditions and to deposition of laminar gypsum and the branching selenite lithofacies, under the control of short term climate fluctuation. Deposition of subunit C (Fig. 14C) reflects most likely continuous restriction and shallowing of the basin, which agrees with the progradational stacking pattern of gypsum layers, that were deposited even in the more distal Govone section. Shallowing and restriction resulted in closer sediment entry points and enhanced sensitivity to riverine runoff, with consequent increase of the input of clay, reduction of gypsum nucleation in the water column and persistent stratification. Stratification is possibly reflected by the partial offset of the $^{18}O_{dol}$ values between sediments deposited in more marginal (Pollenzo section, $^{18}O_{dol}$ as low as –4.9‰ PDB) and deeper sectors (Govone

section, $^{18}O_{dol}$ up to +4.2‰ PDB) of the basin; accordingly, ^{18}O-enriched, denser and likely colder bottom waters occupied the deeper sectors of the basin, whereas ^{18}O-depleted, more diluted and warmer bottom waters were present in more marginal sectors.

No gypsum, but only time equivalent shales, are reported from the buried basin depocenter on the base of seismic data (Ghielmi et al., 2019). This pattern is possibly explained by reduced supply of gypsum from the water column in more open sea and higher rates of bacteria sulfate reduction, deriving from permanent seafloor anoxia and larger availability of organic matter.

6. Conclusions

The analysis of gypsum deposits exposed in the Piedmont Basin provides new insights on the lateral facies transition between the margin and the depocenter of a Messinian marginal subbasin. Bottom-grown gypsum was deposited above the oxycline from overlying saturated brines not affected by bacterial sulfate reduction. Cumulate deposits (laminar gypsum and gypsiferous mudstones) originated from gypsum nucleation at the oxycline and subsequent deposition on an anoxic sea bottom. Deposition of these lithofacies under reducing bottom conditions was controlled by the balance between the rate of sulfate reduction (removing sulfate) and the rate of sulfate replenishment through dissolution of settling gypsum crystals. The branching selenite lithofacies is interpreted as a syngenetic product formed in the sediment at the expenses of dissolved cumulate gypsum. The appearance of cumulate deposits and the branching selenite lithofacies in the 6th PLG cycle (i.e., at about 5.87 Ma) records further restriction of the basin and the intensification of water column stratification. This study suggests that fluctuations of the oxycline in the water mass was a key parameter controlling the stratigraphic distribution of gypsum lithofacies in an ancient stratified basin during the MSC.

ACKNOWLEDGEMENTS

The authors are indebted to Simona Cavagna (University of Torino) for help with SEM observations and to Maria Carmen Valsania (Centre for Nanostructured Interfaces and Surfaces of the University of Torino) for support with FESEM analyses. Juan Peral Lozano (University of Alicante) is thanked for providing the aerial picture of the Pollenzo section (Fig.2). This work was funded by University of Torino grants (ex -60% 2018 and 2019 to F.D. and 2020 to M.N.). Comments and suggestions by the Editor Jasper Knight and two anonymous reviewers helped to improve the quality of the paper.

REFERENCES

Alimi, F., Elfil, H., Gadri, A, 2003. Kinetics of the precipitation of calcium sulfate dihydrate in a desalination unit. Desalination 158, 7–16.

Alimi, F., Gadri, A. 2004. Kinetics and morphology of formed gypsum. Desalination 166, 427–434.

Bąbel, M., 1999. Facies and depositional environments of the Nida Gypsum deposits (Middle Miocene, Carpathian Foredeep, southern Poland). Geological Quarterly 43, 405–428.

Bąbel, M., 2007. Depositional environments of a salina type evaporite basin recorded in the Badenian gypsum facies in northern Carpathian Foredeep. In: Schreiber, B.C., Lugli, S., Bąbel, M. (Eds), Evaporites Through Space and Time. Geological Society of London, Special Publication 285, pp. 107–142.

Bąbel, M., Bogucki, A., 2007. The Badenian evaporite basin of the northern Carpathian Foredeep as a model of a meromictic selenite basin. In: Schreiber, B.C., Lugli, S., Bąbel, M. (Eds), Evaporites Through Space and Time. Geological Society of London, Special Publications 285, pp. 219–246.

Bąbel, M., Schreiber, B.C. 2014. Geochemistry of evaporites and evolution of seawater. In: Holland, H.D., Turekian, K.K. (Eds), Treatise on geochemistry, Second Edition. Elsevier Inc., Amsterdam, pp. 483–560.

Bailey, J.V., Orphan, V.J., Joye, S.B., Corsetti, F., 2009. Chemotrophic microbial mats and their potential for preservation in the rock record. Astrobiology 9, 843–859,

Bigi, G., Cosentino, D., Parotto, M., Sartori, R., Scandone, P., 1990. Structural Model of Italy: Geodinamic Project: Consiglio Nazionale delle Ricerche, S.EL.CA, scale 1:500.000, sheet 1.

Bontognali, T.R.R., Vasconcelos, C., Warthmann, R.J., Lundberg, R., McKenzie, J.A., 2012. Dolomite-mediating bacterium isolated from the sabkha of Abu Dhabi (UAE). Terra Nova 24, 248–254.

Capella, W. Barhoun, N., Flecker, R., Hilgen, F.J., Kouwenhoven, T., Matenco, L.C., Sierro, F.J., Tulbure, M.A., Yousfi, M.Z., Krijgsman, W., 2018. Palaeogeographic evolution of the late Miocene Rifian Corridor (Morocco): reconstructions from surface and subsurface data. Earth-Science Reviews 180, 37-59.

CIESM 2008. The Messinian salinity crisis from mega-deposits to microbiology. In: Briand, F. (Ed.), The Messinian Salinity Crisis from mega-deposits to microbiology - A consensus report, in 33ème CIESM Workshop Monographs 33, pp 1–168.

De Lange, G.J., Krijgsman, W., 2010. Messinian salinity crisis: a novel unifying shallow gypsum/deep dolomite formation mechanism. Marine Geology 275, 273–277.

Dela Pierre, F., Bernardi, E., Cavagna, S., Clari, P., Gennari, R., Irace, A., Lozar, F., Lugli, S., Manzi, V., Natalicchio, M., Roveri, M., Violanti, D., 2011. The record of the Messinian salinity crisis in the Tertiary Piedmont Basin (NW Italy): the Alba section revisited. Palaeogeography, Palaeoclimatology, Palaeoecology 310, 238–255.

Dela Pierre, F., Clari, P., Bernardi, E., Natalicchio, M., Costa, E., Cavagna, S., Lozar, F., Lugli., S., Manzi, V., Roveri. M., Violanti, D., 2012. Messinian carbonate-rich beds of the Tertiary Piedmont Basin (NW Italy): microbially-mediated products straddling the onset of the salinity crisis. Palaeogeography, Palaeoclimatology, Palaeoecology 344, 78–93.

Dela Pierre, F., Natalicchio, M., Ferrando, S., Giustetto, R., Birgel, D., Carnevale, G., Gier, S., Lozar, F., Marabello, D., Peckmann, J., 2015. Are the large filamentous microfossils preserved in Messinian gypsum colorless sulfide-oxidizing bacteria? Geology 43, 855–858.

Dela Pierre F., Natalicchio, M., Lozar, F., Bonetto, S., Carnevale, G., Colombero, S., Sabino, M., Violanti, D., 2016. The Northermost record of the Messinian salinity crisis (Piedmont Basin, NW Italy). Geological Field Trips 8, 1–54.

Dronkert, H., 1985. Evaporite models and sedimentology of Messinian and recent evaporites. GUA papers of Geology. Serials I 24, 283 pp..

Flecker, R., Krijgsman, W., Capella, W., de Castro Martíns, C., Dmitrieva, E., Mayser, J.P., Marzocchi, A., Modestou, S., Ochoa, D., Simon, D., Tulbure, M., van den Berg, B., van der Schee, M., de Lange, G., Ellam, R., Govers, R., Gutjahr, M., Hilgen, F., Kouwenhoven, T., Lofi, J., Meijer, P., Sierro, F.J., Bachiri, N., Barhoun, N., Alami, A.C., Chacon, B., Flores, J.A., Gregory, J., Howard, J., Lunt, D., Ochoa, M., Pancost, R., Vincent, S., Yousfi, M.Z., 2015. Evolution of the Late Miocene Mediterranean–Atlantic gateways and their impact on regional and global environmental change. Earth Science Reviews 150, 365–392.

Fontes, J., Filly, A., Gaudant, J., 1987. Condition de dépôt du Messinien évaporitique des environs d'Alba (Piémont): arguments paléeontologiques et isotopiques. Bollettino Società Paleontologica Italiana 26, 190–210.

Garcìa Veigas, J., Cendòn, D.I., Gibert, L., Lowenstein, T.K., Artiaga, D., 2018.

Geochemical indicators in Western Mediterranean Messinian evaporites: implications for the salinity crisis. Marine Geology 403, 197–214.

Gennari, R., Lozar, F., Natalicchio, M., Zanella, E., Carnevale, G., Dela Pierre, F., 2020. Chronology of the Messinian events in the northernmost part of the Mediterranean: the Govone section (Piedmont Basin, NW italy). Rivista Italiana di Paleontologia e Stratigrafia 126, 541–560.

Ghielmi, M., Rogledi, S., Vigna, B., Violanti, D., 2019. La successione messiniana e plio-pleistocenica del Bacino di Savigliano (Settore occidentale del Bacino Terziario Piemontese) – Italia. Geologia Insubrica 13, 141 pp.

Grothe, A., Andreetto, F., Reichart, G.J, Wolthers, M., Van Baak, C., Vasiliev I., Stoica, M., Sangiorgi, F., Middelburg, J.J., Davies, G.R., Krijgsman, W., 2020. Paratethys pacing of the Messinian Salinity Crisis: low salinity waters contributing to gypsum precipitation? Earth and Planetary Science Letters 542, 116029, hhttps://doi.org/10.1016/j.epsl.2019.116029.

Haq, B., Gorini, C., Baur, J., Moneron, J., Rubino, J.L., 2020. Deep Mediterranean's Messinian evaporite giant: How much salt? Global and Planetary Changes 184, 103052, https://doi.org/10.1016/j.gloplacha.2019.103052.

Hardie, L.A., Eugster, H.P., 1971 The depositional environment of marine evaporites: a case for shallow, clastic accumulation. Sedimentology 16, 187–220.

Hardie, L.A., Lowenstein, T., 2004. Did the Mediterranean Sea dry out during the Miocene? A reassessment of the evaporite evidence from DSDP legs 13 and 42A cores. Journal of Sedimentary Research 74, 453–461.

Hsü, K.J., Cita, M.B.,Ryan, W.B.F., 1973. The origin of the Mediterranean evaporites. In: Ryan, W.B.F., Hsü, K.J., Cita, M.B., Dumitrica, P., Lort, J.M., Mayne, W., Nesteroff

W.D., Pautot, G., Stradner, H., Wezel, F.C. (Eds.), Initial Report of Deep Sea Drilling Program 13. U.S. Government Printing Office, Washington DC, pp. 1203–1231.

Krijgsman, W., Hilgen, F.J., Raffi, I., Sierro, F.J., Wilson, D.S., 1999. Chronology, causes and progression of the Messinian salinity crisis. Nature 400, 652–655.

Irace, A., Dela Pierre, F., Clari, P., 2005. "Normal" and "chaotic" deposits in the Messinian Gessoso-solfifera Fm. at the north eastern border of the Langhe domain (Tertiary Piedmont basin). Bollettino Società Geologica Italiana 4, 77–85.

Lindtke, J., Ziegenbalg, S.B., Brunner, B., Rouchy, J.M., Pierre, C., Peckmann, J., 2011. Authigenesis of native sulphur and dolomite in a lacustrine evaporitic setting (Hellín basin, Late Miocene, SE Spain). Geological Magazine 148, 655–669.

Lofi, J., Sage, F., Déverchère, J., Loncke, L., Maillard, A., Gallier, V., Thinon, I., Gillet, H., Guennoc, P., Gorini, C., 2011. Refining our knowledge of the Messinian salinity crisis records in the offshore domain through multi-site seismic analysis. Bulletin Société Géologique de France 182, 163–180.

Londry, K.L, Des Marais, D.J., 2003. Stable Carbon isotope fractionation by sulfate-reducing bacteria. Applied and Environmental Microbiology 69, 2942–2949.

Lozar, F., Violanti, D., Bernardi, E., Dela Pierre, F., Natalicchio, M., 2018. Identifying the onset of the Messinian salinity crisis: a reassessment of the biochronostratigraphic tools (Piedmont Basin, NW Italy). Newsletters on Stratigraphy 51, 11–31.

Lugli, S., Manzi, V., Roveri, M., Schreiber, B. C., 2010. The Primary Lower Gypsum in the Mediterranean: a new facies interpretation for the first stage of the Messinian salinity crisis. Palaeogeography, Palaeoclimatology, Palaeoecology 297, 83–99.

Lugli, S., Manzi, V., Roveri, M., Schreiber, B.C., 2015. The deep record of the Messinian salinity crisis: evidence of a non-desiccated Mediterranean Sea. Palaeogeography, Palaeoclimatology, Palaeoecology 433, 201–218.

Ma, J., Duan, H., He, L., Tiffany, M., Cao, Z., Qi, T., Shen, M., Biggs, T., Xu, X, 2020. Spatiotemporal pattern of gypsum blooms in the Salton Sea, California during 2000-2018. International Journal of Applied Earth Observation and Geoinformation 89, 102090, https://doi.org/10.1016/j.jag.2020.102090

Manzi, V., Lugli, S., Ricci Lucchi, F., Roveri, M., 2005. Deep-water clastic evaporites deposition in the Messinian Adriatic foredeep (northern Apennines, Italy): did the Mediterranean ever dry out? Sedimentology 52, 875–902.

Manzi, V., Roveri, M., Gennari, R., Bertini, A., Biffi, U., Giunta, S., Iaccarino, S.M., Lanci, L., Lugli, S., Negri, A., Riva, A., Rossi, M.E., Taviani M., 2007. The deep-water counterpart of the Messinian Lower Evaporites in the Apennine foredeep: The Fanantello section (Northern Apennines, Italy). Palaeogeography, Palaeoclimatology, Palaeoecology 251,470–499.

Manzi, V., Gennari, R., Hilgen, F., Krijgsman, W., Lugli, S., Roveri, M., Sierro, F.J., 2013. Age refinement of the Messinian salinity crisis onset in the Mediterranean. Terra Nova 25, 315–322.

Manzi, V., Gennari, R., Lugli, S., Roveri, M., Scafetta, N., Schreiber, B.C., 2012. High-frequency cyclicity in the Mediterranean Messinian evaporites: evidence for solar–lunar climate forcing. Journal of Sedimentary Research 82, 991–1005.

Manzi, V., Lugli, S., Roveri, M., Dela Pierre, F., Gennari, R., Lozar, F., Natalicchio, M., Schreiber, B.C., Taviani, M., Turco, E., 2016. The Messinian salinity crisis in Cyprus: a further step toward a new stratigraphic framework for Eastern Mediterranean. Basin Research 28, 207-236.

Marsaglia, K.M., Tribble, J.S., 1999. Petrography and mineralogy of the uppermost Messinian section and the Pliocene/Miocene boundary at site 975, Western Mediterranean Sea. Proceedings of the Ocean Drilling Program, Scientific Results 161, 3–20.

Meilijson, A., Hilgen, F., Sepulveda, J., Steinberg, J., Fairbank, V., Flecker, R., Waldmann, N., Spaulding, S.A., Bialik, O.M., Boudinot, F.G., Illner, P., Makovsky, Y., 2019. Chronology with a pinch of salt: integrated stratigraphy of Messinian evaporites in the deep Eastern Mediterranean reveals long-lasting halite deposition during Atlantic connectivity. Earth-Science Reviews 194, 374–398.

Miller, K.G., Mountain, G.S., Wright, J.D., Browning, J.V., 2011. A 180-million-year record of sea level and ice volume variations from continental margin and deep-sea isotopic records. Oceanography, 24. 40–53.

Mosca, P., Polino, R., Rogledi, S. Rossi, M., 2010. New data for the kinematic interpretation of the Alps–Apennines junction (Northwestern Italy). International Journal of Earth Sciences 99, 833–849.

Natalicchio, M., Birgel, D., Peckmann, J., Lozar, F., Carnevale, G., Liu, X, Hinrichs, K.U., Dela Pierre, F., 2017. An archaeal biomarker record of paleoenvironmental change across the onset of the Messinian salinity crisis in the absence of evaporites (Piedmont Basin, Italy). Organic Geochemistry 113, 242–253.

Natalicchio, M., Bigel, D., Dela Pierre F., Ziegenbalg, S., Hoffmann-Sell, L., Gier, S., Peckmann, J., 2021. Messinian bottom grown selenitic gypsum: An archive of microbial life. Geobiology, doi. 10.1111/gbi.12464

Ogniben, L., 1957. Petrografìa della Serie Solfifera siciliana e considerazioni geologiche relative. Memorie Descrittive Carta Geologica Italiana 33, 275 pp.

Ortí, F., 2011. Selenite facies in marine evaporites: A review. In: Kendall, C.G., Alsharam, A.S., Jarvis, I., Stevens, T. (Eds), Quaternary carbonate and evaporite sedimentary facies and their ancient analogues: a tribute to Douglas James Shearman. IAS Special Publication 43, pp. 431–464.

Ortí, F., Pueyo Mur, J.J., Geisler-Cussey, D., Dulau, N., 1984. Evaporitic sedimentation in the coastal salinas of Santa Pola (Alicante, Spain). Revista d'Investigacions Geologiques 38, 169–220.

Ortì, F., Rosell, L., Gibert, L., Moragas M., Playa, E., Ingles, M., Rouchy, J.M., Calvo, J.P., Gimeno D., 2014. Evaporite sedimentation in a tectonically active basin: The lacustrine Las Minas Gypsum unit (Late Tortonian, SE Spain). Sedimentary Geology 311, 17–42.

Pellegrino, L., Natalicchio, M., Abe, K., Jordan, R.W., Favero Longo, S., Ferrando, S., Carnevale, G., Dela Pierre, F.,2021. Tiny, glassy and rapidly trapped: the nano-sized planktonic diatoms in Messinian gypsum. Geology 49, doi:10.1130/G49342.1.

Petrash, D.A., Bialik, O.M., Bontognali, R.R., Vasconcelos, C., Roberts, J.A., McKenzie, J.A., Konhauser, K.O., 2017. Microbially catalysed dolomite formation. From near surface to burial. Earth-Sciences Reviews 171, 558 -582

Raad, F., Lofi, J., Maillard, A., Tzevahirzian, A., Caruso, A., 2020. The Messinian Salinity Crisis deposits in the Balearic Promontory: an undeformed analog of the MSC Sicilian basins??, Marine and Petroleum Geology 124, 104777, https://doi.org/10.1016/j.marpetgeo.2020.104777.

Raup, O.B., 1982. Gypsum precipitation by mixing seawater brines. American Association Petroleum Geology Bulletin 66, 363–367.

Reghizzi, M., Lugli, S., Manzi, V., Rossi, F.P., Roveri, M., 2018. Orbitally forced hydrological balance during the Messinian salinity crisis: insights from Strontium isotopes ($^{87}Sr/^{86}Sr$) in the Vena del Gesso Basin (Northern Apennines, Italy). Paleoceanography and Paleoclimatology 33, 716–731.

Reiss, A.G., Gavrieli, I., Ganor, J., 2017. The morphology of gypsum precipitated under hyper-saline conditions – preliminary results from Dead Sea-Red Sea mixtures. Procedia Earth and Planetary Science 17, 376–379.

Rossi, M., 2017. Outcrop and seismic expression of stratigraphic patterns driven by accommodation and sediment supply turnarounds: Implications on the meaning and variability of unconformities in syn-orogenic basins. Marine and Petroleum Geology 87, 112–127.

Rossi, M., Mosca, P., Polino, R., Rogledi, S., Biffi, U., 2009. New outcrop and subsurface data in the Tertiary Piedmont Basin (NW-Italy): unconformity-bounded stratigraphic units and their relationships with basin-modification phases. Rivista Italiana di Paleontologia e Stratigrafia 115, 305–335.

Rouchy, J.M., Caruso, A., 2006. The Messinian salinity crisis in the Mediterranean basin: A reassessment of the data and an integrated scenario. Sedimentary Geology 188–189, 35–67.

Roveri, M., Flecker, R., Krijgsman, W., Lofi, J., Lugli, S., Manzi, V., Sierro, F.J., Bertini, A., Camerlenghi, A., De Lange, G., Govers, R., Hilgen, F.J., Hübscher, C., Meijer, P.T., Stoica, M.., 2014. The Messinian Salinity Crisis: Past and future of a great challenge for marine sciences. Marine Geology 352, 25–58.

Roveri, M., Lugli, S., Manzi, V., Reghizzi, M., Rossi, F.P., 2020. Stratigraphic relationships between shallow-water carbonates and primary gypsum: insights from the Messinian succession of the Sorbas Basin (Betic Cordillera, Southern Spain). Sedimentary Geology 404, 105678, https://doi.org/10.1016/j.sedgeo.2020.105678

Ryan, W.B.F., 2008. Modeling the magnitude and timing of evaporite drawdown during the Messinian salinity crisis. Stratigraphy 5, 227–243.

Sabino, M., Dela Pierre, F., Natalicchio, M., Birgel, D., Gier, S., Peckmann, J., 2021. The response of water column and sedimentary environments to the advent of the Messinian salinity crisis: insights from an onshore deepwater section (Govone, NW Italy). Geological Magazine 158, 825-841.

Sanz-Montero, M.E., Rodríguez-Aranda, J.P., García del Cura, M.A., 2009. Bioinduced precipitation of barite and celestite in dolomite microbialites: examples from Miocene lacustrine sequences in the Madrid and Duero Basins, Spain. Sedimentary Geology 222, 138–148.

Schreiber, B.C., El Tabakh, M., 2000. Deposition and early alteration of evaporites. Sedimentology 47, 215–238.

Schreiber, B.C., Friedman, G.M., Decima, A., Schreiber, E., 1977. Depositional environments of Upper Miocene (Messinian) evaporite deposits of the Sicilian Basin. Sedimentology 23, 729–760.

Shearman, D. J., Ortí Cabo, F., 1976. Upper Miocene gypsum: San Miguel de Salinas, SE Spain. Memorie della Società Geologica Italiana 16, 327–340.

Simon, D., Meijer, P.T., 2017. Salinity stratification of the Mediterranean Sea during the Messinian crisis: A first model analysis. Earth and Planetary Science Letters 479, 366–376.

Sturani, C., 1973. A fossil eel (*Anguilla* sp.) from the Messinian of Alba (Tertiary Piedmontese Basin). Palaeoenvironmental and palaeogeographic implications. In: Drooger C.W. (Ed.): Messinian events in the Mediterranean. Koninklijke Nederlandse Akademie van Wetenschappen, Geodynamics Science Report 7, pp. 243–255.

Sturani, C., Sampò, M., 1973. Il Messiniano inferiore in facies diatomitica nel Bacino Terziario Piemontese. Memorie della Società Geologica Italiana 12, 335–338.

Tiffany, M.A., Ustin, S.L., Hurlbert, S.H., 2007. Sulfide irruptions and gypsum blooms in the Salton Sea as detected by satellite imagery, 1979–2006. Lake and Reservoir Management 23, 637–652.

Torfstein, A., Gavrieli, I., Stein, M. 2005, The sources and evolution of sulfur in the hypersaline Lake Lisan (paleo Dead Sea). Earth and Planetary Science Letters 236, 61–77.

Trenkwalder, S., Violanti, D., d'Atri, A., Lozar, F., Dela Pierre, F., Irace, A., 2008. The Miocene/Pliocene boundary and the Early Pliocene micropaleontological record: new data from the Tertiary Piedmont Basin (Moncucco quarry, Torino Hill, Northwestern Italy). Bollettino Società Paleontologica Italiana 47, 87–103.

Van der Laan, E., Hilgen, F.J., Lourens, L.J., de Kaenel, E., Gaboardi, S., Iaccarino, S., 2012. Astronomical forcing of Northwest African climate and glacial history during the late Messinian (6.5–5.5 Ma). Palaeogeography, Palaeoclimatology, Palaeoecology 313, 107–126.

Van Lith, Y., Warthmann, R., Vasconcelos, C., McKenzie, J., 2003. Sulphate reducing bacteria induce low temperature Ca-dolomite and high Mg-calcite formation. Geobiology 1, 71–79.

Vasconcelos, C., McKenzie, J.A., Bernasconi, S., Grujic, D., Tien, A.J., 1995. Microbial mediation as a possible mechanism for natural dolomite formation at low temperature. Nature 377, 220–222.

Violanti, D., Dela Pierre, F., Trenkwalder, S., Lozar, F., Clari, P., Irace, A., d'Atri, A., 2011. Biostratigraphic and palaeoenvironmental analyses of the Messinian/Zanclean boundary and Zanclean succession in the Moncucco quarry (Piedmont, northwestern Italy). Bulletin de la Société Géologique de France 182, 149–162.

Violanti, D., Lozar, F., Dela Pierre, F., Natalicchio, M., Bernardi, E., Clari, P., Cavagna, S., 2013. Stress tolerant microfossils of a Messinian succession from the northern Mediterranean basin (Pollenzo section, Piedmont, Northwestern Italy). Bollettino Società Paleontologica Italiana 52, 45–54.

Wakeham, S.G., Amann, R., Freeman, K.H., Hopmans, E.C., Jørgensen, B.B., Putnam, I.F., Schouten, S., Sinninghe Damsté, J.S., Talbot, H.M., Woebken, D., 2007. Microbial

ecology of the stratified water column of the Black Sea as revealed by a comprehensive biomarker study. Organic Geochemistry 38, 2070–2097.

Warthmann, R., van Lith, Y., Vasconcelos, C., McKenzie, J.A., Karpoff, A.M., 2000. Bacterially induced dolomite precipitation in anoxic culture experiments. Geology 28, 1091–1094.

FIGURE AND TABLE CAPTIONS

Table 1

Total Organic Carbon (TOC) contents, dolomite contents, $^{13}C_{dol}$ and $^{18}O_{dol}$ values of representative samples.

Fig. 1

(A) Distribution of Messinian evaporites in the Mediterranean basin (modified from Manzi et al., 2013). (B) Chronostratigraphic framework of the Messinian salinity crisis (modified from Manzi et al., 2013). (C) Structural sketch map of the Piedmont Basin (modified from Bigi et al., 1990) with location of the stratigraphic sections shown in Fig. 3 (numbers): (1) Arnulfi; (2) Pollenzo; (3) Monticello; (4) Castagnito; (5) Govone. TH: Torino Hill; MO: Monferrato; gray dotted lines indicate the isobaths of the base of Pliocene deposits. The black dotted line is the trace of the cross section shown in panel D. (D) Schematic cross section showing the distribution of the Messinian sediments (from Dela Pierre et al., 2011), with locations of the stratigraphic sections mentioned in the text (numbers). The trace of the cross section is indicated in panel C. M/P: Miocene-Pliocene boundary. PLG: Primary Lower Gypsum unit; RLG: Resedimented Lower Gypsum unit; UG: Upper Gypsum; MES: Messinian erosional surface.

Fig. 2

(A) Aerial view of the Pollenzo section, showing the lithological cycles of the PLG unit. More competent layers correspond to gypsum, softer layers to shales. The white rectangle indicates the position of panel B; (B) Detail of A.

Fig. 3

Correlation scheme of the sections cited in the text (see Fig. 1C for their location). Datum plane: base of the Sturani key-bed. SAF: Sant'Agata Fossili Marls; PLG: Primary Lower Gypsum unit; MES: Messinian erosional surface. PLG1-PLG 15: Primary Lower Gypsum cycle.

Fig.4

Subunit A. (A) The gypsum layer of cycle PLG5, composed of massive selenite, and the overlying cycle PLG 6 with the Sturani key-bed (Pollenzo section). (B) Dm-sized vertically-oriented twinned selenite crystal from cycle PLG5 (Pollenzo section). (C) Banded selenite lithofacies (cycle PLG4, Arnulfi section); the yellow dotted lines indicate clay layers between crystal palisades. (D) m-scale gypsum cone composed of vertically-oriented selenite crystals (cycle PLG5, Castagnito section). The yellow dotted line indicates the base of the cones, the white dotted lines indicate bedding of hosting shales.

Fig.5

Sturani key-bed in the Arnulfi (A) and Monticello (B, C) sections. Note in (A) the coalescent nodular aggregates (arrows) growing in laminar gypsum (white lines) and a large asymmetric cone (yellow dotted line); in (C), laminar gypsum (LG) and the branching selenite (BS)

lithofacies are clearly visible. Note that the branching selenite is formed by clusters of nodular aggregates.

Fig. 6

Laminar gypsum (LG) and branching selenite (BS). (A) A m-scale branch, internally composed of smaller nodular aggregates (arrows) above laminar gypsum (Pollenzo section). (B) Close up of the laminar gypsum; note the cm-thick packets separated by clay-rich layers (Pollenzo section). (C) Detail of B, showing a five cm-thick laminated packet, bordered by clay-rich layers (arrows). The gypsum-rich laminae are typified by a whitish to pinkish colour. (D) The laminar gypsum in the Monticello section.

Fig. 7

(A) Plane view of the Sturani key-bed in the Pollenzo section: note the large asymmetrical cone (yellow dotted lines) and the elongation of the more developed arm (branch) towards the left side of the picture (south). (B) Transversal view of the same branch of (A) (yellow dotted line). Note that the laminae in the laminar gypsum (white dotted lines) can be traced within the branch where they are oblique to the bedding. The sketch on the left side indicates the 3D shape of the cone and the orientation of the thin sections shown in Fig. 12A-C. (C) Meter-sized conical structures at the base of the Sturani key-bed in the Pollenzo section, observed from below. (D) Aerial view of asymmetrical cones. (E) Detail of (D), showing clusters of nodular aggregates parallel to the elongation of a branch (arrows). (F) Detail of (E), showing mm-sized gypsum crystals with their long axis oriented parallel to the elongation of a branch.

Fig. 8

(A) Stratigraphic log and outcrop view of the Sturani key-bed in the Pollenzo section, showing the stratigraphic relationships between laminar gypsum (LG) and the branching selenite (BS) lithofacies. A large branch cross-cutting laminar gypsum (yellow dotted lines) is visible. The thick black lines in the log indicate clay-rich layers which subdivide the Sturani key-bed in twelve gypsum-rich intervals. (B) Bended and deformed laminae (arrows) around the nodular aggregates. (C) Detail of (A), showing the draping of the laminae on the upward termination of a branch (white dotted line). Note the nodular aggregates composing the branch.

Fig. 9

Gypsiferous mudstones. (A) Outcrop view of cycle PLG7 (Pollenzo section). Note the lamination in the gypsiferous mudstones and the small cones they enclose (arrows). (B) A single cone enclosed in gypsiferous mudstones (Cycle PLG15, Govone section). The X, Y and Z axes refer to the orientation of the sections reported in (C). (C) Transversal and planar section of the same cone of (B); arrows indicate the growth direction of the crystals. Note the radial distribution of the crystals.

Fig. 10

Photomicrographs in transmitted (A, B) and UV-light (C) of vertically-oriented twinned selenite crystals (subunit A). (A) Alternation of turbid and limpid laminae in the re-entrant angle of the twin. (B) Turbid lamina (TL) and light lamina (LL) from the same crystal of (A). The red arrows indicate the filamentous microfossils. (C) Fluorescent clay-rich aggregates corresponding to marine snow floccules. Note the tiny pyrite grains in the center.

Fig. 11

Laminar gypsum (subunit B). (A, B) Photomicrographs in transmitted light. Note that thicker gypsum-rich laminae are separated by thin clay-rich laminae. (C) Close-up of a gypsum lamina (polarized light): note the sutured boundaries in two large crystals (arrow). (D, E) Photomicrographs in transmitted (D) and UV (E) light of a cut slightly oblique to lamination. Note in (D) the random orientation of the gypsum crystals and in (E) the high autofluorescence of a clay-rich lamina. Pollenzo section. (F) Backscatter SEM image of the clay-rich matrix between the gypsum crystals (gy). Note the silt-size terrigenous grains (t) and the abundant, bright grains corresponding to pyrite (arrows). Pollenzo section. (G) SEM image of a clay-rich lamina showing clustered dolomite microcrystals with rounded shape and hollow core and some terrigenous grains (t). Monticello section. (H) SEM image of dolomite microcrystals with hollow core.

Fig. 12:

Branching selenite (subunit B). (A) Transmitted light photomicrograph of a cut perpendicular to the elongation of the branch represented in Fig. 7B; nodular crystal aggregates separated by thin strings of sediment are recognizable. (B) UV-light photomicrograph showing a detail of (A). Note the zoned crystal typified by a fluorescent core and a non-fluorescent rim and the high fluorescence of the surrounding clay-rich sediment. (C) Plane view of the branch represented in Fig. 7B (transmitted light photomicrograph); note that the crystals (arrows) are disposed parallel to the elongation of the branch; the inset shows a twinned crystal. (D) Transmitted light photomicrograph of a cut parallel to the elongation of the branch (Fig. 7B). The crystals (arrows) are disposed parallel to the elongation of the branch as in (C). Nodular crystal aggregates are recognizable. (E, G) Photomicrographs in transmitted (E) and UV (F) light of interlocked crystals composing the nodular aggregates; note the solid inclusions (peloids) in the core of the crystals (arrows) and in (F) the different fluorescence intensity of

the core (c) and the rim (r). (G) Elongated prismatic primary gypsum crystal (arrow) enclosed in a larger crystal (polarized light). The yellow faces of the rectangle in panels A, C and D indicate the orientation of the thin sections (see also Fig. 7B).

Fig. 13

Gypsiferous mudstones (subunit C). (A) Alternation of gypsum-rich and gypsum-poor laminae. Note the larger size of the crystals compared to laminar gypsum. (B) Nodular aggregates composed of interlocked crystals.

Fig. 14

Schematic representation of the depositional conditions of the three subunits composing the PLG unit. (A) Subunit A (vertically-oriented crystals); (B) Subunit B (laminar gypsum and branching selenite; (C) Subunit C (gypsiferous mudstones). The panel below (B) shows the interpreted mode of deposition of laminar gypsum (steps 1 and 2) and the branching selenite lithofacies (step 3). The light blue arrow on the right indicates the influx of Mediterranean (Med) water in the basin. See text for details.

Sample	Section	PLG cycle	Lithofacies	TOC (%)	Dolomite (wt%)	$\delta^{13}C_{dol}$	$\delta^{18}O_{dol}$
Ar1	Arnulfi	PLG6 (SKB)	Laminar gypsum	n.a.	-	-2,4	-4,9
SKB-A2	Pollenzo	PLG6 (SKB)	Laminar gypsum	0.97	5.3	-2,4	-2,9
PDZ5.7	Pollenzo	PLG8	Gypsiferous mudstones	2,03	29.9	-2,3	+3,9
PDZ6.9	Pollenzo	PLG9	Gypsiferous mudstones	1,03	11.2	-4,2	+1,9
PDZ7.8	Pollenzo	PLG10	Gypsiferous mudstones	1,50	11.8	-2,9	-4,2
PDZ8.4	Pollenzo	PLG11	Gypsiferous mudstones	1,18	9.9	+0,1	-4,9
SG-M7	Govone	PLG8	Gypsiferous mudstones	n.a.	28.7	-3,0	+4,2
SG-M10	Govone	PLG9	Gypsiferous mudstones	n.a.	21.7	-2,3	+3,8
PDZ.3.10	Pollenzo	PLG6 (SKB)	Branching selenite	0,14	n.a.		
PDZ.3.12	Pollenzo	PLG6 (SKB)	Branching selenite	0,22	n.a		
PDZ.3.15	Pollenzo	PLG6 (SKB)	Branching selenite	0,13	n.a.		
PDZ.3.16	Pollenzo	PLG6 (SKB)	Branching selenite	0,08	n.a.		
PDZ.4.12	Pollenzo	PLG7	Branching selenite	0,17	n.a.		
PDZ.4.13	Pollenzo	PLG7	Branching selenite	0,41	n.a.		
PDZ.5.8	Pollenzo	PLG8	Branching selenite	0,10	n.a.		
PDZ.6.10	Pollenzo	PLG9	Branching selenite	0,18	n.a.		
PDZ.6.8	Pollenzo	PLG9	Branching selenite	0,18	n.a.		
PDZ.7.8	Pollenzo	PLG10	Branching selenite	0,08	n.a.		
PDZ.7.9	Pollenzo	PLG10	Branching selenite	0,08	n.a.		
PDZ.8.5	Pollenzo	PLG11	Branching selenite	0,23	n.a.		
PDZ.9.5	Pollenzo	PLG12	Branching selenite	0,39	n.a.		

n.a.: not analyzed

Declaration of interests

☒ The authors declare that they have no known competing financial interests or personal relationships that could have appeared to influence the work reported in this paper.

☐The authors declare the following financial interests/personal relationships which may be considered as potential competing interests:

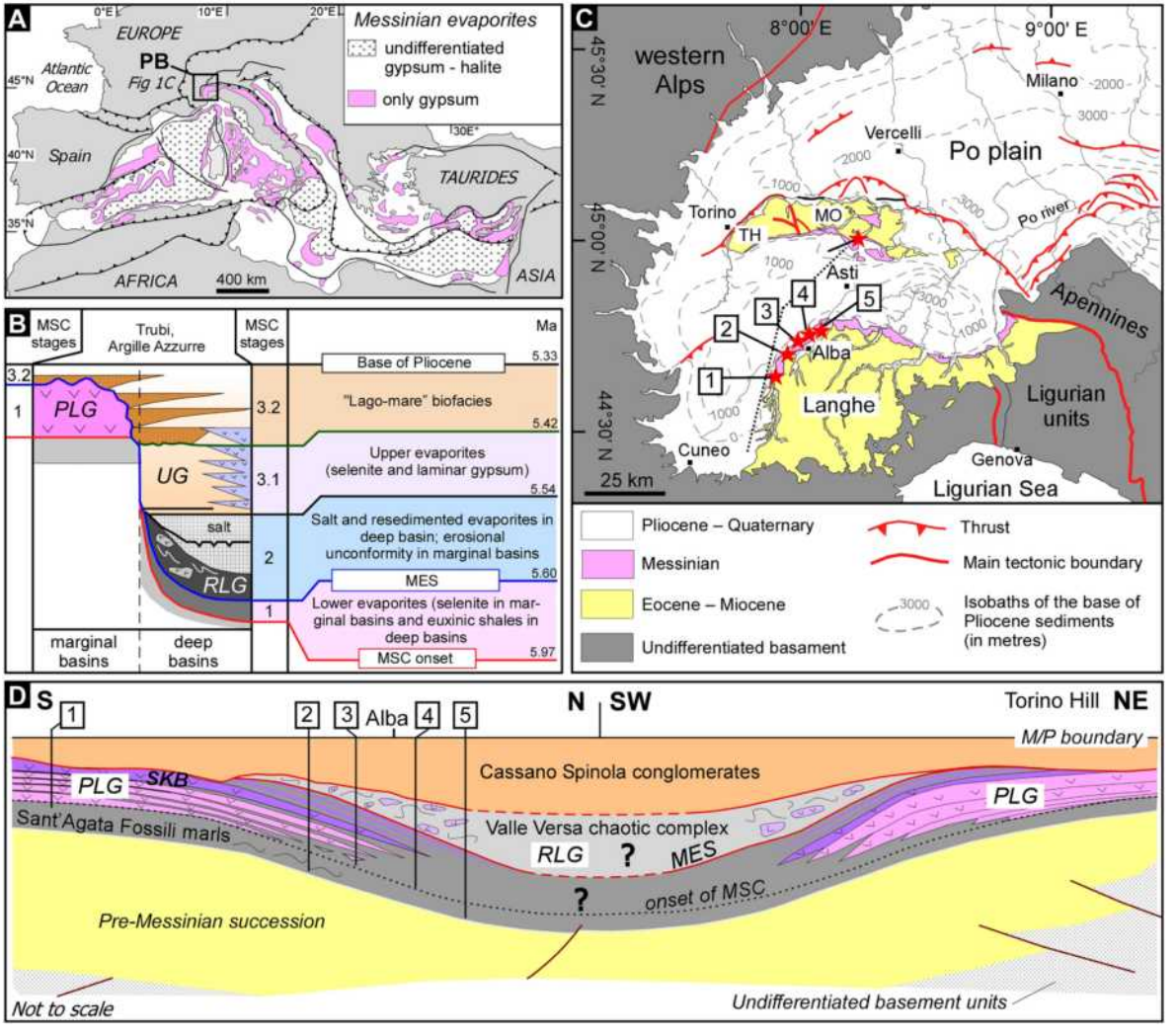
A
EUROPE
PB
Fig 1C
Atlantic Ocean
Spain
AFRICA
TAURIDES
ASIA
400 km
Messinian evaporites
undifferentiated gypsum - halite
only gypsum
B
MSC stages
Trubi, Argille Azzurre
MSC stages
Ma
Base of Pliocene
5.33
"Lago-mare" biofacies
5.42
Upper evaporites (selenite and laminar gypsum)
5.54
Salt and resedimented evaporites in deep basin; erosional unconformity in marginal basins
MES
5.60
Lower evaporites (selenite in marginal basins and euxinic shales in deep basins
MSC onset
5.97
PLG
UG
RLG
salt
marginal basins
deep basins
C
western Alps
Po plain
Milano
Vercelli
Torino
TH
MO
Asti
Alba
Langhe
Cuneo
Genova
Ligurian Sea
Ligurian units
Apennines
Po river
25 km
Pliocene – Quaternary
Messinian
Eocene – Miocene
Undifferentiated basament
Thrust
Main tectonic boundary
Isobaths of the base of Pliocene sediments (in metres)
D
S
N
SW
Torino Hill
NE
M/P boundary
PLG
SKB
Sant'Agata Fossili marls
Cassano Spinola conglomerates
Valle Versa chaotic complex
RLG
MES
onset of MSC
Pre-Messinian succession
Undifferentiated basement units
Not to scale

Figure 1

Figure 2

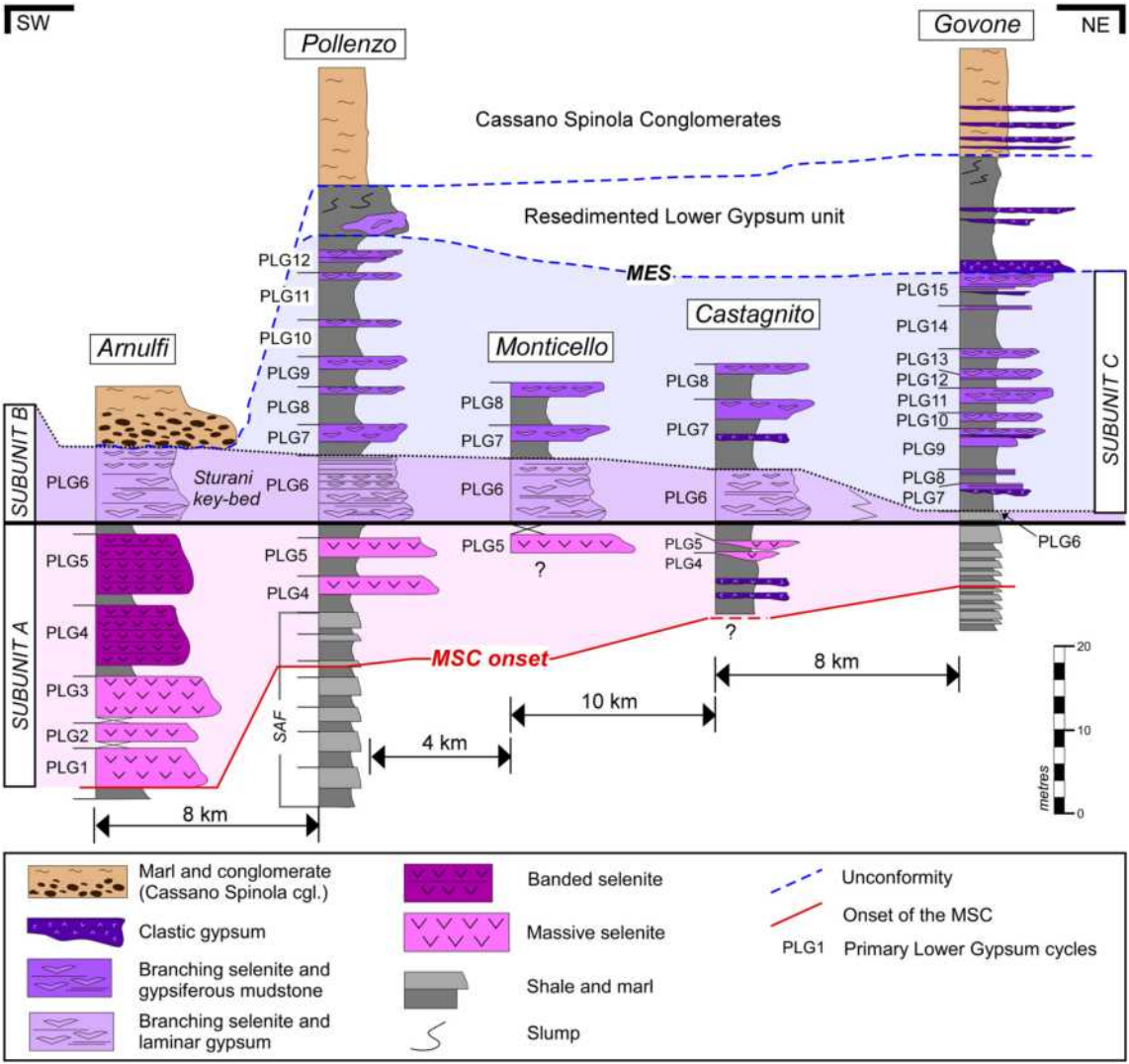
SW
NE
Pollenzo
Govone
Cassano Spinola Conglomerates
Resedimented Lower Gypsum unit
MES
Amulfi
Monticello
Castagnito
SUBUNIT B
SUBUNIT C
SUBUNIT A
Sturani key-bed
PLG15
PLG14
PLG13
PLG12
PLG11
PLG10
PLG9
PLG8
PLG7
PLG6
PLG5
PLG4
PLG3
PLG2
PLG1
?
MSC onset
SAF
8 km
4 km
10 km
8 km
20
10
0
metres
Marl and conglomerate (Cassano Spinola cgl.)
Clastic gypsum
Branching selenite and gypsiferous mudstone
Branching selenite and laminar gypsum
Banded selenite
Massive selenite
Shale and marl
Slump
Unconformity
Onset of the MSC
PLG1 Primary Lower Gypsum cycles

Figure 3

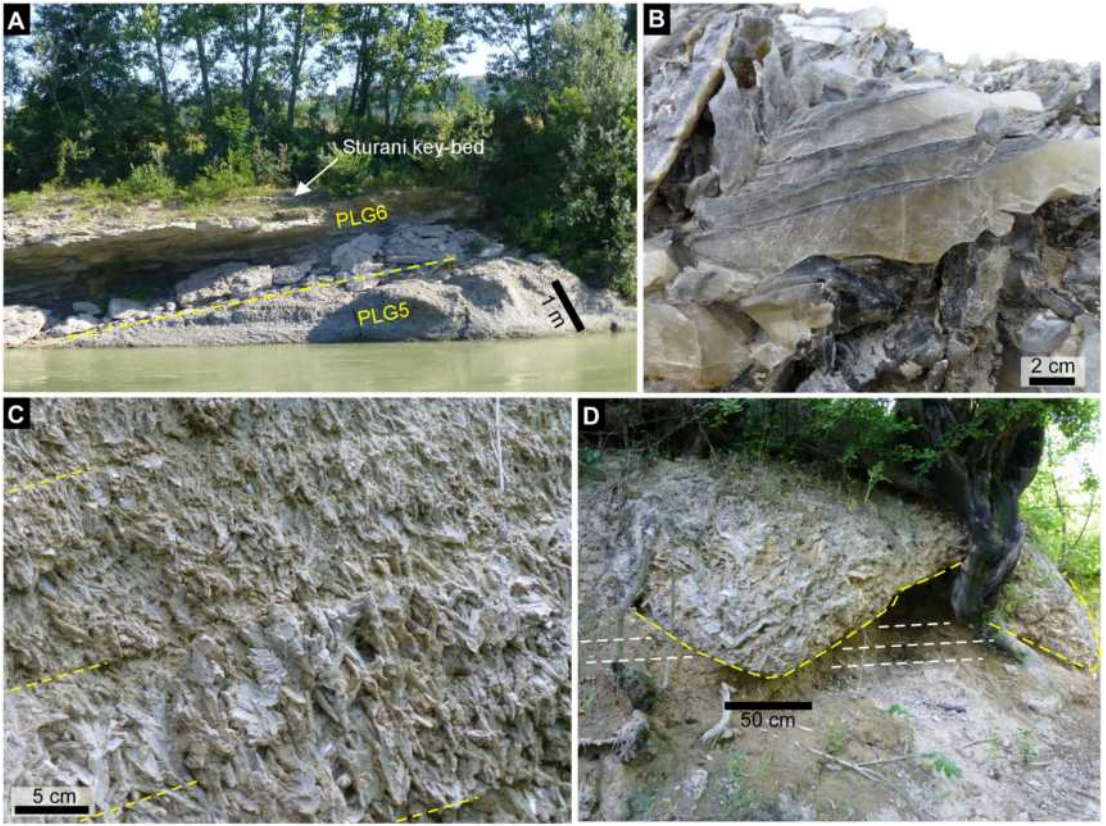

Figure 4

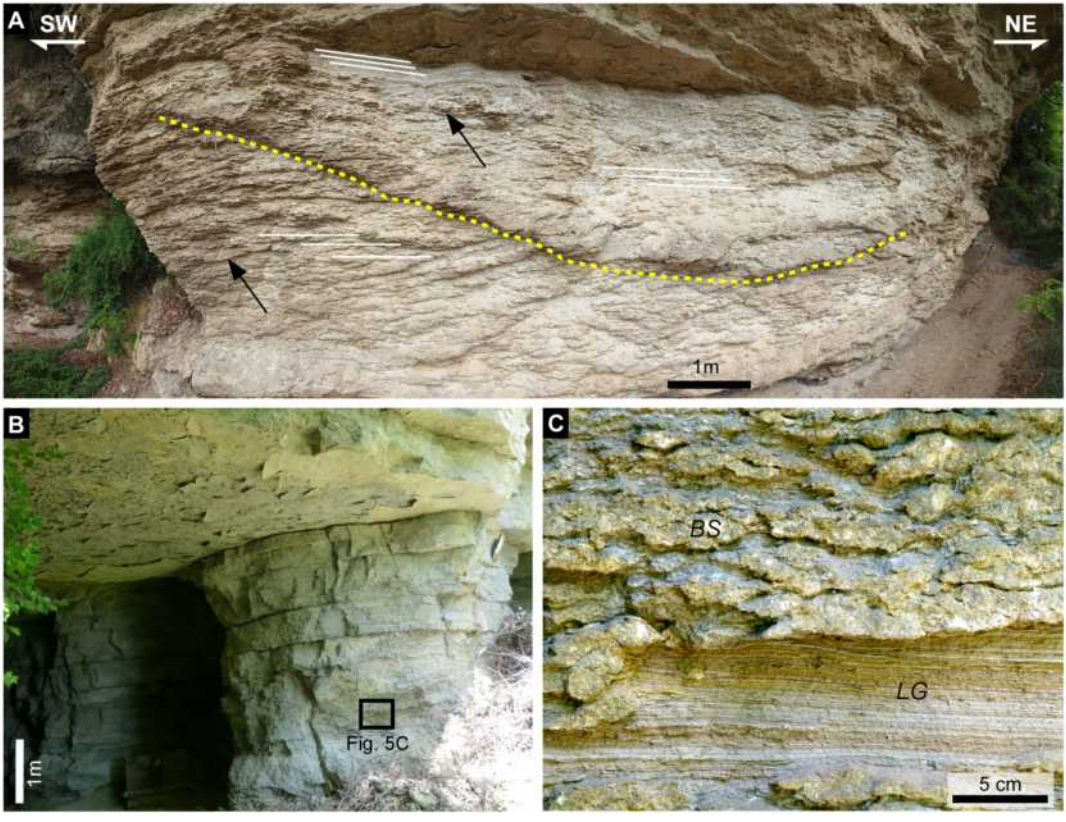

Figure 5

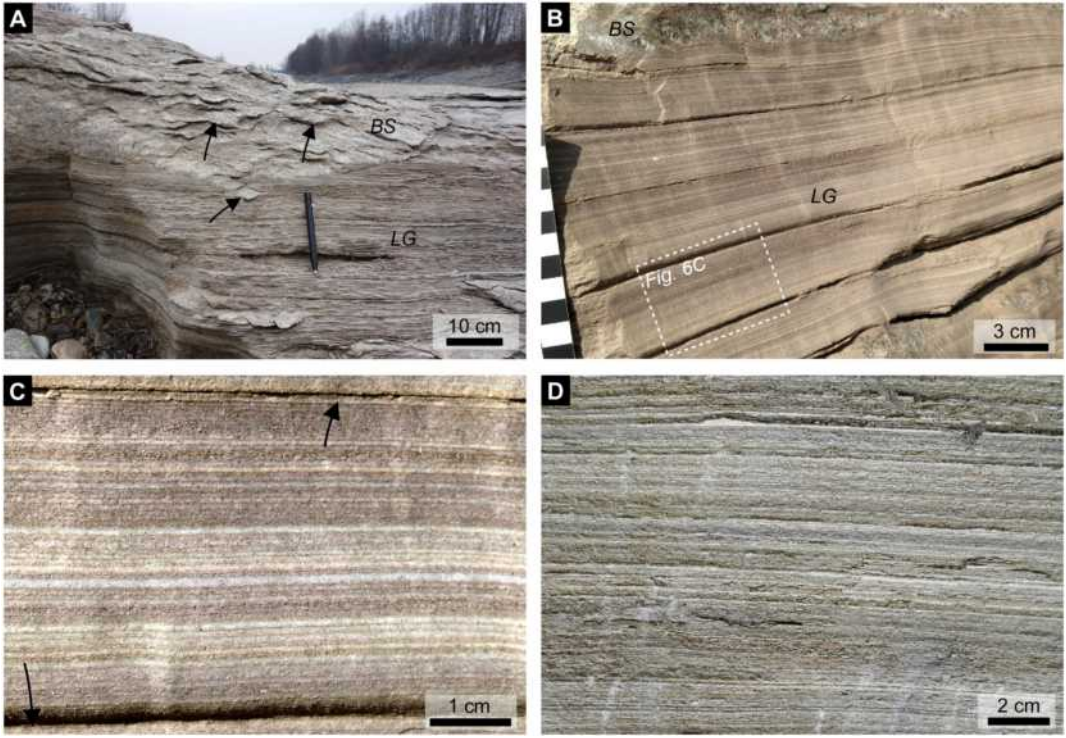

Figure 6

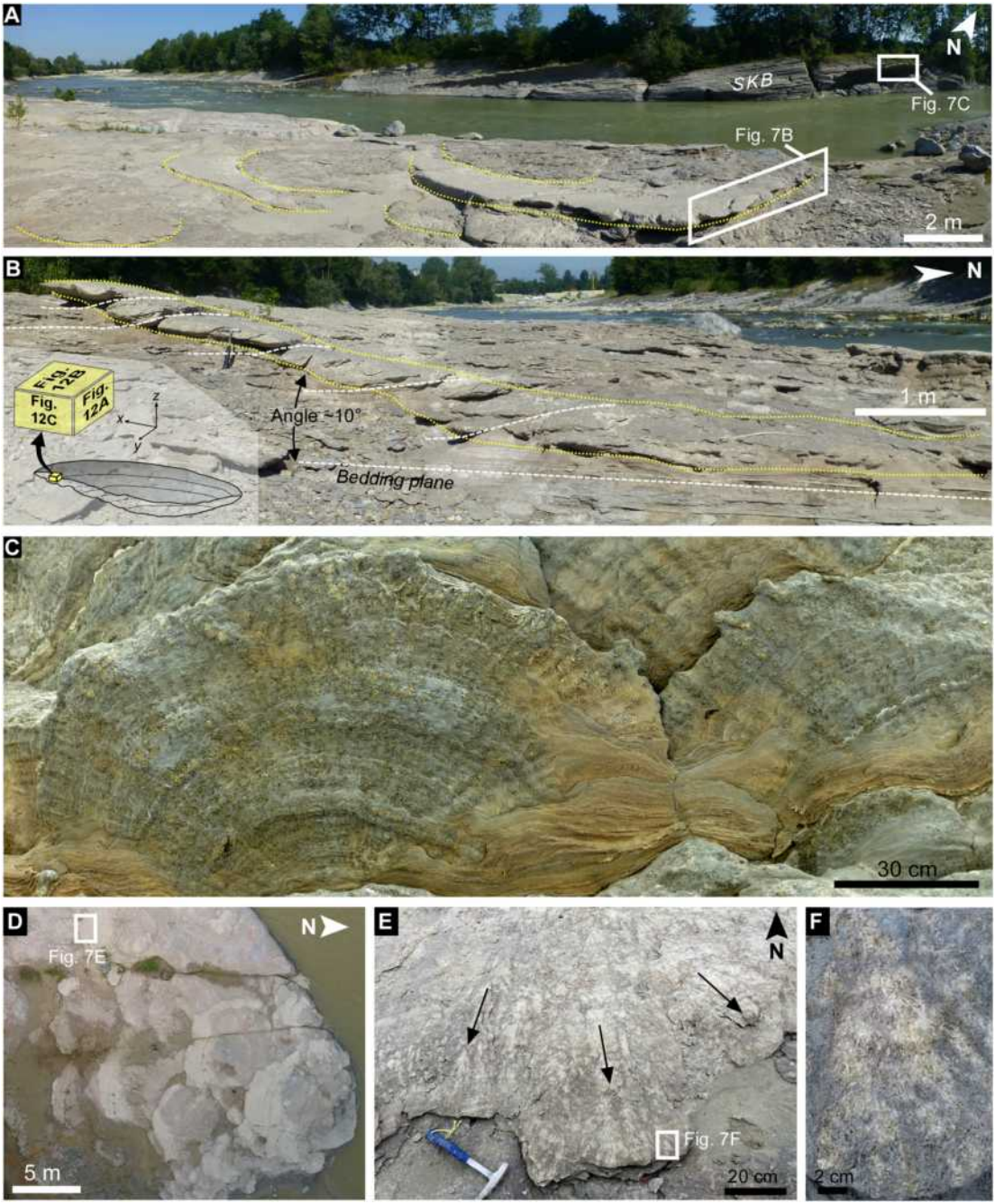
A
N
SKB
Fig. 7C
Fig. 7B
2 m
B
N
Fig. 12B
Fig. 12C
Fig. 12A
z
x
y
Angle ~10°
Bedding plane
1 m
C
30 cm
D
Fig. 7E
N
5 m
E
N
Fig. 7F
20 cm
F
2 cm

Figure 7

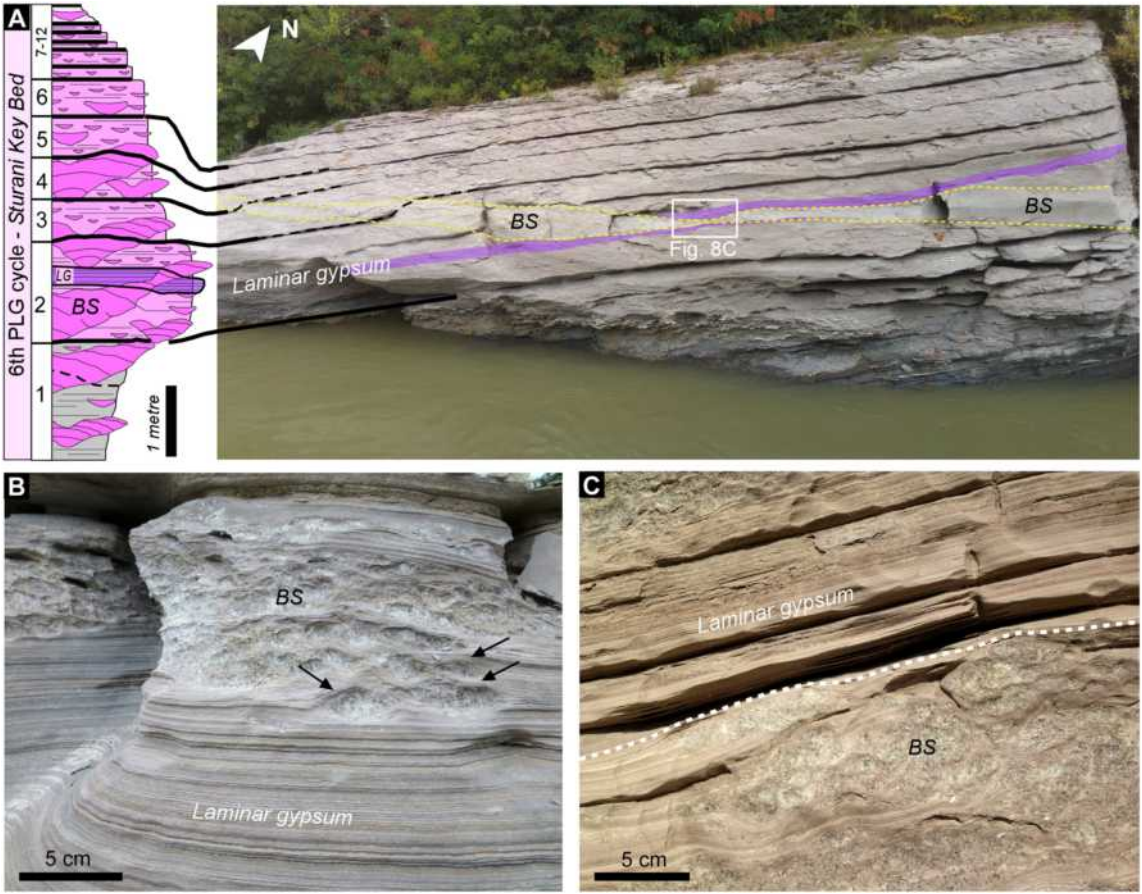
A
6th PLG cycle - Sturani Key Bed
7-12
6
5
4
3
LG
2
BS
1
1 metre
N
BS
Fig. 8C
BS
Laminar gypsum
B
BS
Laminar gypsum
5 cm
C
Laminar gypsum
BS
5 cm

Figure 8

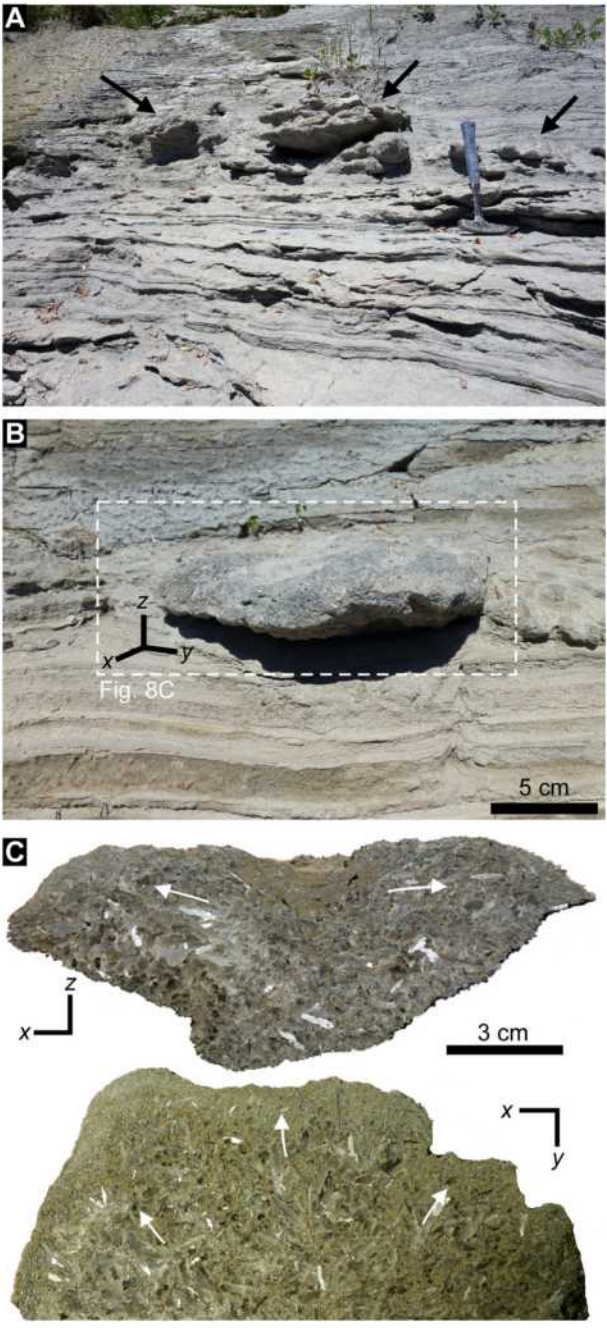

Figure 9

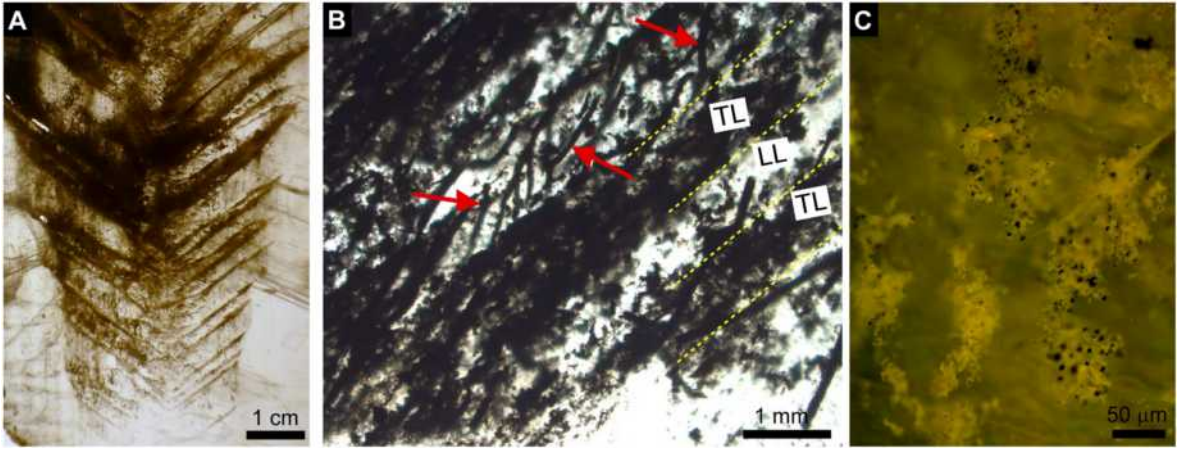

Figure 10

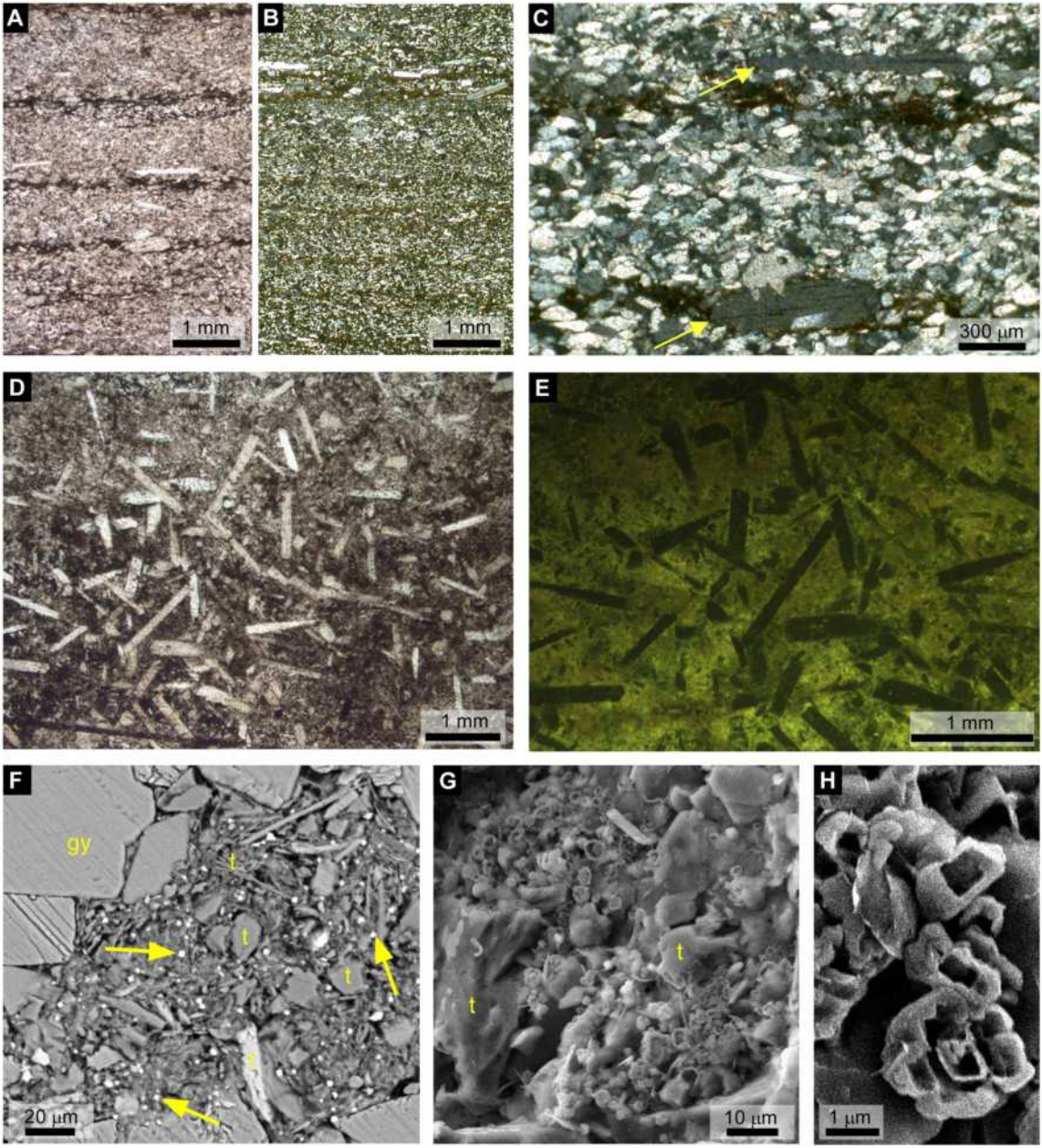

Figure 11

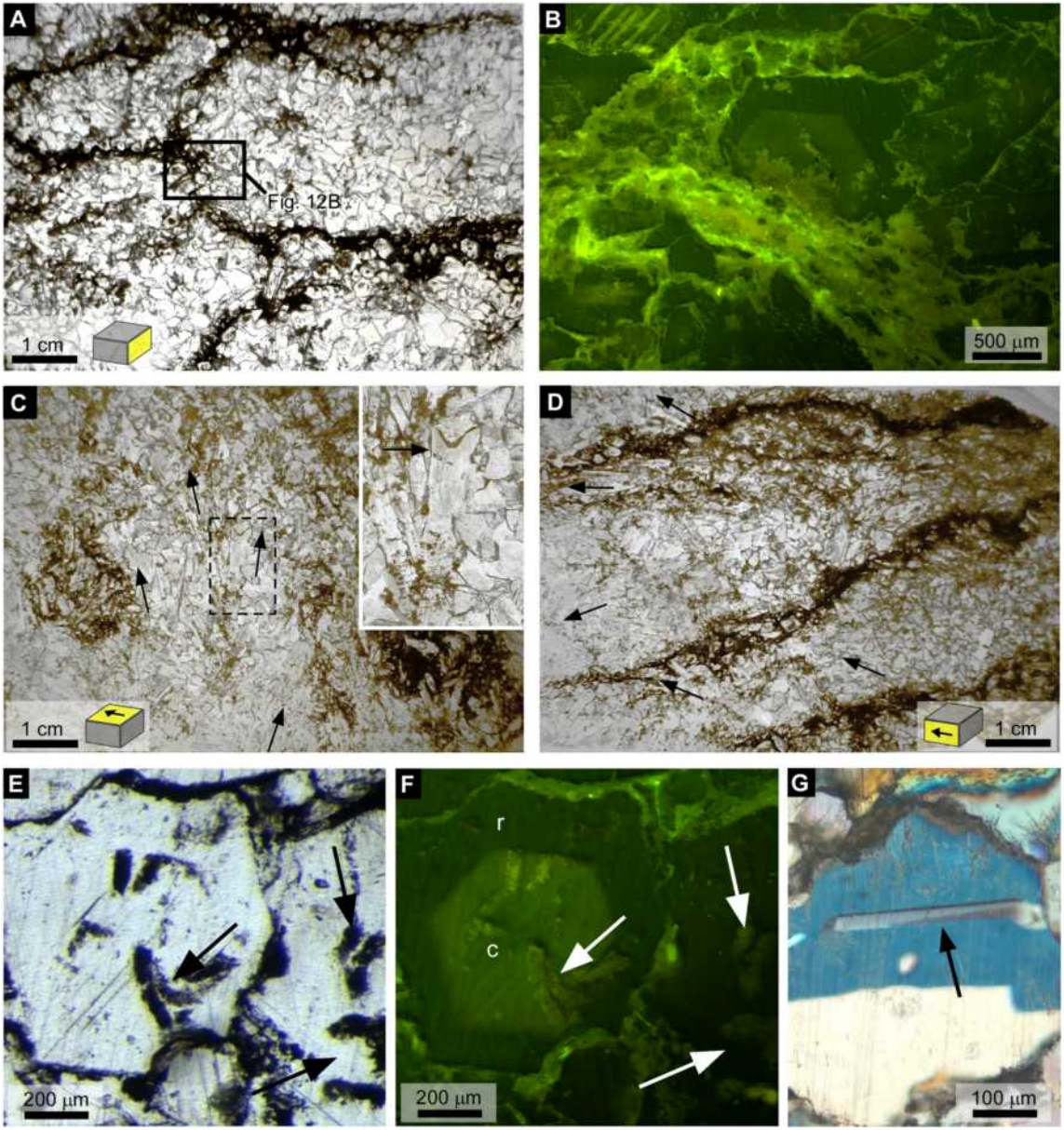

Figure 12

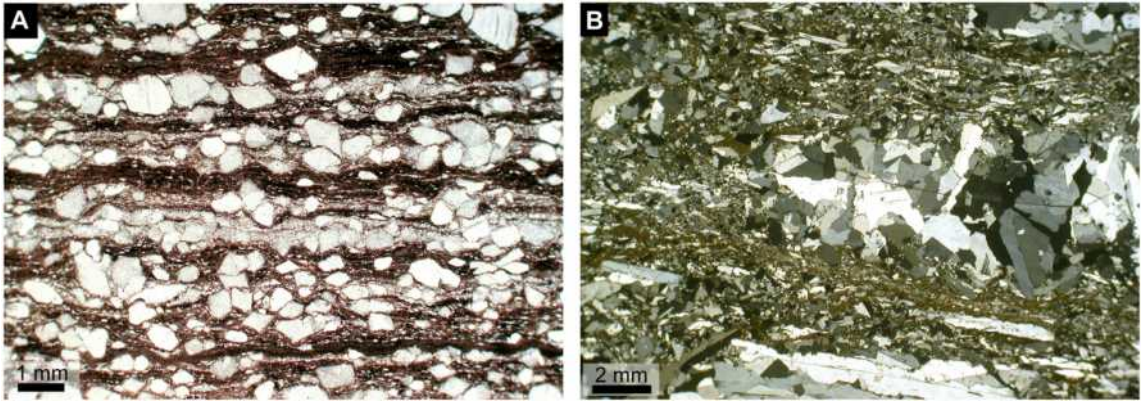

Figure 13

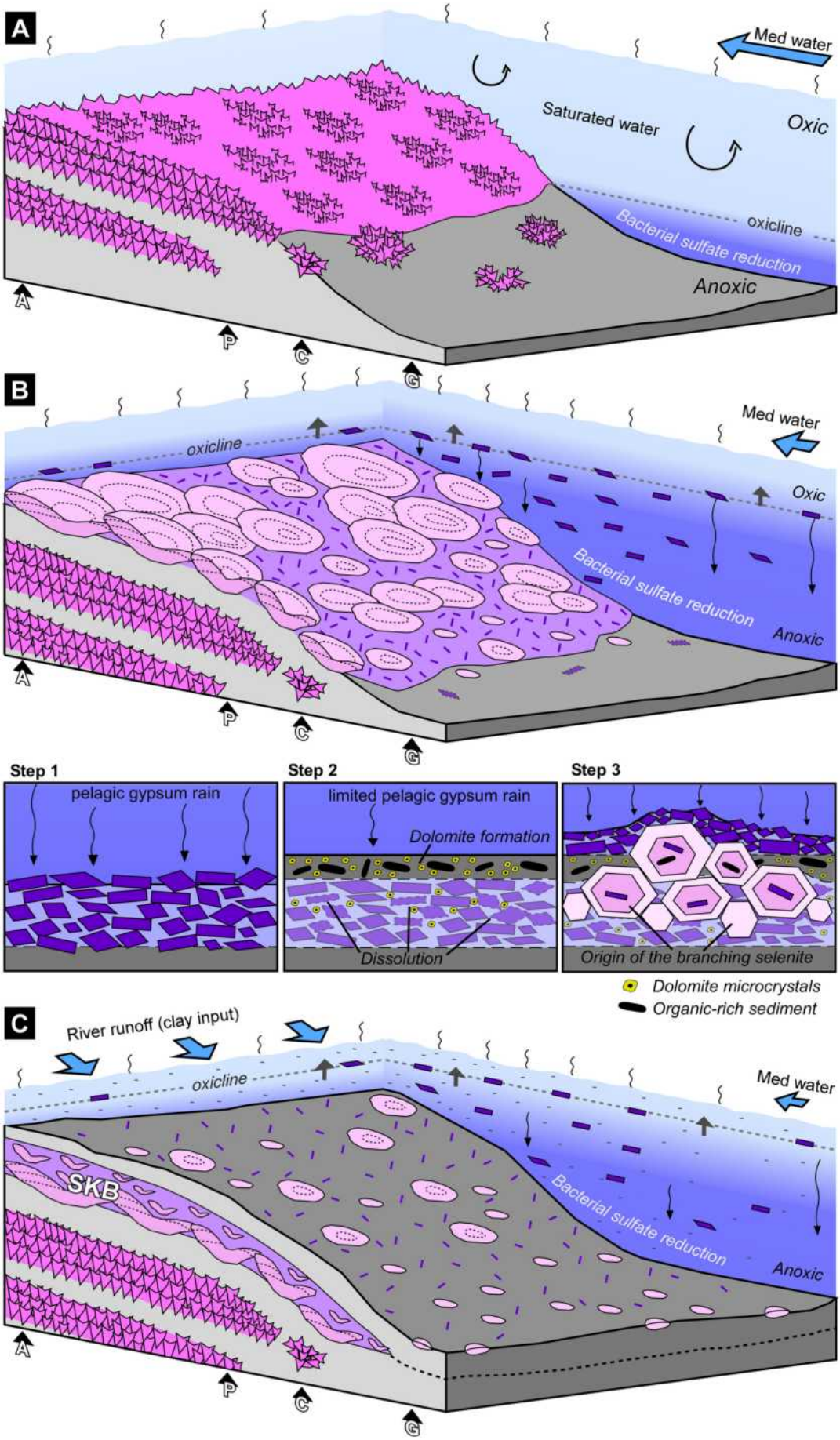
A
Med water
Saturated water
Oxic
oxicline
Bacterial sulfate reduction
Anoxic
A
P
C
G
B
Med water
oxicline
Oxic
Bacterial sulfate reduction
Anoxic
A
P
C
G
Step 1
pelagic gypsum rain
Step 2
limited pelagic gypsum rain
Dolomite formation
Dissolution
Step 3
Origin of the branching selenite
Dolomite microcrystals
Organic-rich sediment
C
River runoff (clay input)
oxicline
Med water
SKB
Bacterial sulfate reduction
Anoxic
A
P
C
G

Figure 14